Simulated Climate and Climate Change in the GFDL CM2.5 High-Resolution Coupled Climate Model

THOMAS L. DELWORTH, ANTHONY ROSATI, AND WHIT ANDERSON

NOAA/Geophysical Fluid Dynamics Laboratory, Princeton, New Jersey

ALISTAIR J. ADCROFT AND V. BALAJI

Princeton University, Princeton, New Jersey

RUSTY BENSON, KEITH DIXON, AND STEPHEN M. GRIFFIES

NOAA/Geophysical Fluid Dynamics Laboratory, Princeton, New Jersey

HYUN-CHUL LEE

NOAA/Geophysical Fluid Dynamics Laboratory, Princeton, New Jersey, and High Performance Technologies, Inc., Reston, Virginia

RONALD C. PACANOWSKI,* GABRIEL A. VECCHI, ANDREW T. WITTENBERG, FANRONG ZENG, AND RONG ZHANG

NOAA/Geophysical Fluid Dynamics Laboratory, Princeton, New Jersey

(Manuscript received 7 June 2011, in final form 7 October 2011)

ABSTRACT

The authors present results for simulated climate and climate change from a newly developed high-resolution global climate model [Geophysical Fluid Dynamics Laboratory Climate Model version 2.5 (GFDL CM2.5)]. The GFDL CM2.5 has an atmospheric resolution of approximately 50 km in the horizontal, with 32 vertical levels. The horizontal resolution in the ocean ranges from 28 km in the tropics to 8 km at high latitudes, with 50 vertical levels. This resolution allows the explicit simulation of some mesoscale eddies in the ocean, particularly at lower latitudes.

Analyses are presented based on the output of a 280-yr control simulation; also presented are results based on a 140-yr simulation in which atmospheric CO_2 increases at 1% yr^{-1} until doubling after 70 yr.

Results are compared to GFDL CM2.1, which has somewhat similar physics but a coarser resolution. The simulated climate in CM2.5 shows marked improvement over many regions, especially the tropics, including a reduction in the double ITCZ and an improved simulation of ENSO. Regional precipitation features are much improved. The Indian monsoon and Amazonian rainfall are also substantially more realistic in CM2.5.

The response of CM2.5 to a doubling of atmospheric CO_2 has many features in common with CM2.1, with some notable differences. For example, rainfall changes over the Mediterranean appear to be tightly linked to topography in CM2.5, in contrast to CM2.1 where the response is more spatially homogeneous. In addition, in CM2.5 the near-surface ocean warms substantially in the high latitudes of the Southern Ocean, in contrast to simulations using CM2.1.

1. Introduction

Climate models are the primary tools for making predictions about the future state of the climate system. It is an important goal of climate science to continually improve these models to increase our confidence in the

* Retired.

Corresponding author address: Thomas L. Delworth, NOAA/GFDL, P.O. Box 308, Princeton University, Princeton, NJ 08542. E-mail: tom.delworth@noaa.gov

DOI: 10.1175/JCLI-D-11-00316.1

prediction of future climate states. The fidelity and utility of climate models are limited in several key respects, including (i) incomplete knowledge of the physical, chemical and biological processes that govern the behavior of the climate system, and (ii) constraints on computational resources that limit the ability both to simulate small-scale processes (such as atmospheric convection and clouds) and to simulate climate on regional spatial scales. This latter limitation is especially troublesome, since oftentimes it is on these smaller spatial scales that climate change information is most needed.

Here we present simulated climate and climate change from a newly developed climate model of much finer resolution than previous climate models used at the National Oceanic and Atmospheric Administration's (NOAA) Geophysical Fluid Dynamics Laboratory (GFDL). The improved representation of some smaller-scale processes in the climate system appears to substantially improve the simulation of many key aspects of climate, and is thus an important advance. The present work builds on, and is complementary to, efforts at other institutions to build high-resolution coupled models. For example, Shaffrey et al. (2009) present results from a Hadley Centre model in which the ocean has a 1/3° horizontal resolution and the atmosphere has a horizontal resolution of approximately 1°. Their results show significant improvements in simulating many aspects of the climate system. Similarly, Gent et al. (2010) show improvements in the mean state from a version of the National Center for Atmospheric Research (NCAR) Community Climate System Model (CCSM) with an atmospheric resolution of 0.5°. In particular, regional precipitation patterns and their associated river outflows are more realistic than in a coarser-resolution version. Bryan et al. (2010) demonstrate that the nature of air–sea coupling can be very different at high horizontal resolutions. McClean et al. (2011) show the explicit simulation of tropical cyclones in a high-resolution global coupled model, and the changing character of Agulhas eddies. Kirtman et al. (2011, manuscript submitted to *Climate Dyn.*) use a high-resolution version of the NCAR CCSM to assess the impact of ocean eddies on the mean state, variability, and nature of ocean–atmosphere interactions. Sakamato et al. (2011, manuscript submitted to *J. Meteor. Soc. Japan*) also show improvements with a high-resolution coupled model, especially for orographic effects and coastal upwelling.

2. Model formulation

The model development documented in this paper started from the GFDL Climate Model version 2.1 (CM2.1; Delworth et al. 2006, hereafter referred to as D06) that was widely used and analyzed as part of the Intergovernmental Panel on Climate Change (IPCC) Fourth Assessment Report (AR4). This model is still widely used, and output from a large set of experiments is freely available (see http://nomads.gfdl.noaa.gov/CM2.X/). The aim of the current effort is to assess how simulations of climate variability and change are altered when the model horizontal resolution is substantially refined, and physical and numerical formulations consistent with that resolution are employed. This grid refinement permits both simulation of phenomena on smaller spatial scales, and improved representation of physical processes in the climate system that operate on smaller spatial scales. We refer to this new higher-resolution model as GFDL CM2.5v1 (where ''v1'' denotes that this is version 1 of this model; we will refer to this model as simply CM2.5 in the remainder of this paper, with the v1 implicit).

One goal of this model development was to construct a model that had very different characteristics than our previous models, and was effectively in a new part of the ''parameter space'' of global coupled climate models. For the ocean component of the coupled model we made a conscious decision to build a model that had no explicit lateral diffusion, used viscosity that was as small as numerically possible, and used a highly accurate formulation for advection (see below) that minimizes numerical diffusion. The combination of these factors allows the model to simulate very energetic oceanic flows, including intense boundary currents. We also chose not to use a parameterization of the effects of oceanic mesoscale eddies in this first version of CM2.5, but rather to allow the model to try to simulate eddies explicitly. Although the grid resolution of CM2.5 (discussed below) is insufficient to fully resolve oceanic eddies, especially at higher latitudes, we chose this model development pathway to facilitate an assessment of the role of oceanic eddies in the climate system, and to minimize parameterized processes. As shown below, the comparison of our models, CM2.5 and CM2.6, can shed light on the role of ocean eddies, and will be the subject of future work (CM2.6 will be described briefly in section 2f below).

a. Atmospheric component

The atmospheric component of CM2.5 is derived from the atmospheric component of GFDL CM2.1 (Delworth et al. 2006). The horizontal resolution has been refined from roughly 200 km in CM2.1 to approximately 50 km in CM2.5. The atmospheric component is formulated on a ''cubed-sphere'' grid (Lin 2004; Putman and Lin 2007), in which the spherical atmosphere is represented on six sides of a cube. This formulation avoids the numerical problem of the convergence of meridians at the poles and associated filtering, and allows grid boxes of roughly equal area over the globe.

The parameterized atmospheric physics are nearly identical to those described in GFDL Global Atmospheric Model Development Team (2004) and D06, with the exception of some tuning of cloud parameters to achieve a radiative balance at the finer spatial resolution. In addition, there are 32 levels in the vertical, as opposed to the 24 levels used in CM2.1. The extra levels are mainly concentrated in the upper troposphere and lower stratosphere.

b. Oceanic component

The ocean model is substantially different from that used in CM2.1, previously described in D06, Griffies et al. (2005), and Gnanadesikan et al. (2006). The ocean grid in CM2.5 is considerably finer, with horizontal spacing varying from 28 km at the equator to 8–11 km at high latitudes, in contrast to the spacing of approximately 100 km used in CM2.1. In addition, the grid boxes maintain an aspect ratio close to 1, in contrast to CM2.1 where the aspect ratio can exceed 2 at high latitudes because of the convergence of the meridians. Both CM2.5 and CM2.1 use a ''tri-polar'' grid (Murray 1996), in which there are displaced poles located over northern Canada and Russia to avoid a singularity at the North Pole. The ocean component for both CM2.1 and CM2.5 uses 50 levels in the vertical.

In addition to finer resolution than in CM2.1, the following are characteristics of the ocean component of CM2.5:

- CM2.5 does not use a parameterization for the effects of mesoscale eddies [in contrast to CM2.1, which uses a parameterization as described in Griffies et al. (2005) and Gnanadesikan et al. (2006)].
- CM2.5 uses a parameterization for the effects of submesoscale, mixed layer eddies (Fox-Kemper et al. 2011).
- CM2.5 uses a third-order finite volume advection scheme—the piecewise parabolic method (PPM). PPM reconstructs the subgrid-scale variation of scalar fields using piecewise polynomials that are bounded and limited to be monotonic. High-order interpolation of edge values increases the effective accuracy for the small Courant–Friedrichs–Lewy number. PPM is widely used and the use of PPM here is motivated by the need to significantly improve ocean climate models, which require advection to be conservative, monotonic, and highly accurate (Colella and Woodward 1984; Huynh 1996). This scheme is more accurate and less dissipative than that used in CM2.1.
- There is no explicit lateral diffusion in CM2.5, and there is no prescribed background vertical diffusion.
- Vertical mixing in CM2.5 is determined by the *K*-profile parameterization (KPP) scheme from Large et al. (1994), in addition to the coastal tide mixing scheme of Lee et al. (2006). CM2.5 also employs the internal tide mixing scheme of Simmons et al. (2004).
- CM2.5 uses the Modular Ocean Model version 4.1 (MOM4.1) code (Griffies 2010) and a z^* vertical coordinate (see the appendix of Griffies et al. 2011).
- CM2.5 uses very low viscosity with the Smagorinsky biharmonic formulation (Griffies and Hallberg 2000) and a prescribed background viscosity that is enhanced next to western boundaries.
- All straits connecting bodies of water (such as the Atlantic and the Mediterranean) have explicit flow, rather than the parameterized exchange used in CM2.1.

The sum of these changes creates an ocean component in CM2.5 that is far more energetic than the ocean component of CM2.1. The higher-order advection scheme, finer horizontal resolution, and lack of explicit diffusion mean that sharp gradients in both the horizontal and vertical are maintained, such as associated with boundary currents and the thermocline (shown below).

c. Land component

The land model in CM2.5 is called LM3 (P. C. D. Milly et al. 2011, unpublished manuscript) and represents a major change over the land model used in CM2.1. LM3 is a new model for land water, energy, and carbon balance. In comparison to its predecessor [the Land Dynamics (LaD) model (Milly and Shmakin 2002)], LM3 includes a multilayer model of snowpack above the soil; a continuous vertical representation of soil water that spans both the unsaturated and saturated zones; a frozen soil–water phase; a parameterization of water-table height, saturated-area fraction, and groundwater discharge to streams derived from standard groundwater-hydraulic assumptions and surface topographic information; finite-velocity horizontal transport of runoff via rivers to the ocean; lakes, lake ice, and lake-ice snow packs that exchange mass and energy with both the atmosphere and the rivers; and consistent, energy-conserving accounting of the sensible heat content of water in all its phases. In stand-alone numerical experiments with observation-based atmospheric forcing, LM3 preserves the generally realistic water-balance partitioning of the LaD model, ameliorates some of the deficiencies of the LaD model previously identified, and provides qualitatively realistic estimates of physical variables that are not tracked by the LaD model.

d. Sea ice component

The sea ice component used in CM2.5 is almost identical to that used in CM2.1, called the GFDL Sea Ice Simulator (SIS). SIS is a dynamical model with three

vertical layers, one snow and two ice, and five ice-thickness categories. The elastic–viscous–plastic technique (Hunke and Dukowicz 1997) is used to calculate ice internal stresses, and the thermodynamics is a modified Semtner three-layer scheme (Winton 2000). Details of the model formulation and configuration are given in appendix 1 of D06. The only difference from the sea ice model used in CM2.1 is that the albedos are higher than in CM2.1, and are closer to the central value of observational estimates from Perovich et al. (2002). Specifically, the maximum albedo of snow on sea ice increased from 0.80 in CM2.1 to 0.85 in CM2.5, and the maximum albedo of sea ice increased from 0.58 in CM2.1 to 0.68 in CM2.5.

The details of the flow of ice from continental regions into the ocean, including ice shelves and their interaction with the ocean, are beyond the scope of this model. Therefore, CM2.5 incorporates a recently developed parameterization of the effects of icebergs on the coupled climate system (Martin and Adcroft 2010), in which the movement of snow from the continent into the ocean causes the formation of a statistical distribution of icebergs. These icebergs move away from the coasts, driven by winds and currents, and eventually melt and deposit their freshwater into the ocean while maintaining a global hydrologic balance. Further details are in Martin and Adcroft (2010).

Even with this iceberg parameterization, one of the model shortcomings is that at this resolution some of the complexity of the coastal regions of Antarctica and Greenland is captured, but the model is not able to fully represent all of the relevant processes. For example, sea ice forms in some of the small semi-enclosed bays on the Antarctic and Greenland coasts. However, the narrowness of the passageways connecting these bays to the open ocean inhibits the movement of this ice to the open ocean where it could melt. The ice in some of these inlets can be effectively trapped, and continues to grow as more ice is formed. This trapping can result in the localized growth of sea ice to hundreds of meters in a few such isolated bays; this unrealistic growth reflects model limitations.

e. Coupling characteristics and model time steps

The model ocean and atmosphere exchange fluxes once every hour, and are thus able to represent a diurnal cycle in coupling characteristics. In addition, the surface current speeds are taken into account when computing wind stresses on the ocean (Pacanowski 1987). The time step is 20 min for most atmospheric physics, but is 3 h for radiation. The ocean time step is 30 min.

f. Simulations

A number of simulations from both models are examined. For CM2.1 we use the following experiments:

- CM2.1_1990_Control: a 300-yr simulation with atmospheric composition (greenhouse gases, aerosols) and external forcing (solar irradiance) fixed at 1990 levels
- CM2.1_1990_Control_NO_GM: a 100-yr simulation identical to the 1990 control for CM2.1, except that there is no parameterization of the effects of mesoscale eddies in the ocean

For CM2.5 we use the following experiments:

- CM2.5_1990_Control: a 280-yr simulation with atmospheric composition (greenhouse gases, aerosols) and external forcing (solar irradiance) fixed at 1990 levels
- CM2.5_2X_CO_2: a 140-yr simulation that starts from year 101 of the 1990 control simulation, but in which atmospheric CO_2 increases at a rate of 1% yr^{-1} until reaching double its initial value after 70 yr, and is held fixed thereafter

When calculating the model's response to doubled CO_2, it is common to start the doubled CO_2 simulation from a long control simulation with an 1860 atmospheric composition; such an ''1860 Control'' simulation produces a climate that may be closer to a radiative balance, since the atmospheric composition is closer to preindustrial conditions. However, such 1860 control simulations can take many centuries to come into balance, and CM2.5 is very computationally expensive. Therefore, we used our 1990 control simulation as the starting point for the CM2.5_2X_CO_2 simulation.

To make a clean comparison with CM2.1, we also need a 2X_CO_2 simulation of CM2.1 that starts from a 1990 control simulation. This had not been done previously (the 2X_CO_2 simulation with CM2.1 had been done from an 1860 control simulation), so a new pair of simulations was conducted. However, the computer system had changed since the original CM2.1 simulations were conducted, and thus we were not able to precisely replicate the original CM2.1. In addition, several minor code bugs had been discovered, and those had been corrected. Therefore, for the 2X_CO_2 runs with CM2.1, we used a slightly different version of CM2.1 than what we used for the IPCC AR4. This version of CM2.1 also uses values of albedo over sea ice that are higher than the original CM2.1, but identical to CM2.5. This slightly revised version of CM2.1 can be referred to as ''CM2.1v2''. In this paper we use output from the revised version of CM2.1 to compare the CO_2 responses of CM2.1 and CM2.5, but use the original version of CM2.1 for comparing the time-mean state and most of the internal variability between CM2.1 and CM2.5.

A comparison of the original and new versions of CM2.1 (not shown) confirms that the climates are quite similar. Further, we also have available a 2X_CO_2 run

with the original version of CM2.1, but starting from an 1860 control simulation; the response to increasing CO_2 is broadly similar in the original and revised versions of CM2.1, but with a slightly larger amplitude in the revised version of CM2.1. This is likely associated with the higher values of albedo over sea ice (see above) used in the revised version. Since the original and revised versions of CM2.1 are broadly similar in both their control simulations and response to CO_2, we still refer to this revised model in the text as CM2.1.

Therefore, for estimating the response of CM2.1 to a doubling of CO_2, we use the following experiments that were conducted with the revised version of CM2.1:

- CM2.1_1990_Control: a 240-yr simulation with atmospheric composition (greenhouse gases, aerosols) and external forcing (solar irradiance) fixed at 1990 levels
- CM2.1_2X_CO_2: a 140-yr simulation that starts from year 101 of the 1990 control simulation, but in which atmospheric CO_2 increases at a rate of 1% yr^{-1} until reaching double its initial value after 70 yr, and is held fixed thereafter

We will also make use of an additional prototype higher-resolution climate model, GFDL CM2.6. This model has the same atmosphere as CM2.5, and identical ocean physics as CM2.5. The CM2.6 ocean component has substantially higher horizontal resolution than CM2.5, with grid spacing varying from 11 km at the equator to less than 4 km at very high latitudes. As shown below, CM2.6 simulates a very realistic distribution of ocean eddy activity. Because of the computational expense of this model we have only performed a 30-yr 1990 control simulation, but the comparison with CM2.5 helps to illuminate some of the physical factors responsible for the biases present in CM2.5, with particular emphasis on the role of ocean eddies.

To derive the ocean initial conditions for the 1990 control integration, a 1-yr integration of the ocean component of the coupled model (CM2.1, CM2.5, or CM2.6) is conducted starting from observed climatological conditions [taken from Steele et al. (2001), which is an extension of Antonov et al. (1998) and Boyer et al. (1998)], with the ocean initially at rest. The ocean model is forced with surface fluxes (Griffies et al. 2009); in addition, surface temperature and salinity are restored to the Steele et al. (2001) climatology with a 10-day restoring time scale. The purpose of the 1-yr run is to avoid any potential shocks that might arise from initializing the coupled model using an ocean at rest, and to generate a large-scale ocean circulation prior to coupling to the atmosphere. Output from the end of that 1-yr spinup is taken as the initial condition for the coupled run. The atmospheric initial conditions are taken from the end of an atmosphere–land simulation with prescribed SSTs.

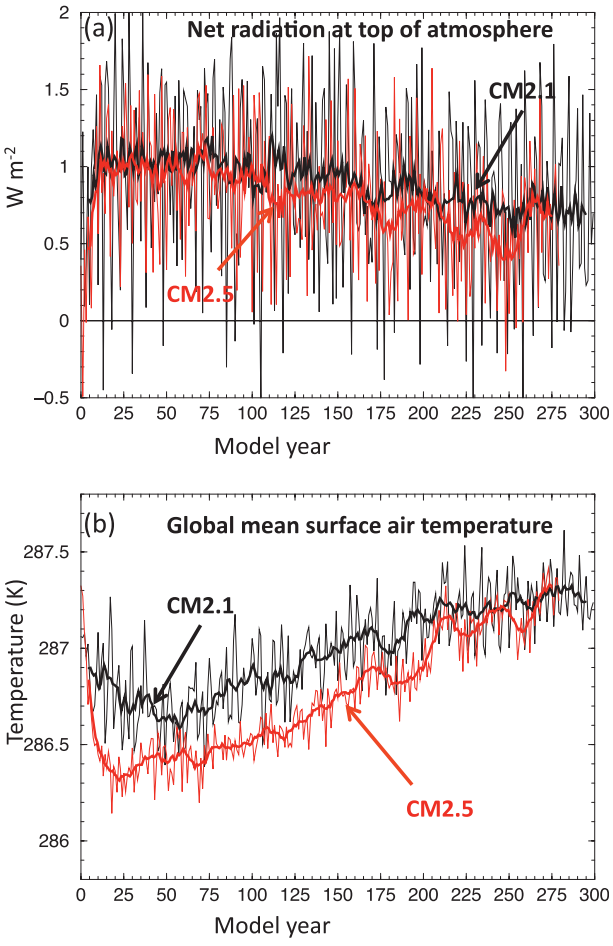

FIG. 1. Model results from 1990 control simulations using CM2.1 and CM2.5. (a) Time series of global mean, annual mean net radiation at the top of the atmosphere. Units are W m^{-2}. Thin black (red) lines are yearly values for CM2.1 (CM2.5) while thick black (red) lines are smoothed with a 10-yr running mean. (b) As in (a), but for near-surface air temperature.

3. Simulation characteristics

a. Model drift

We first examine the temporal drift of the 1990 control simulations. Shown in Fig. 1a are the time series of the annual mean, global mean net radiation at the top of the atmosphere. For both models there is a rapid initial increase to slightly more than 1 W m^{-2}, after which there is a slow decline over the following centuries (positive values indicate more radiation entering the earth's climate system than exiting to space). This imbalance is reflected in a long-term increase in ocean heat content.

Shown in Fig. 1b are the time series of annual mean, global mean surface air temperature. For both models there is an initial cooling over the first several decades, with greater cooling in CM2.5 than CM2.1. As discussed

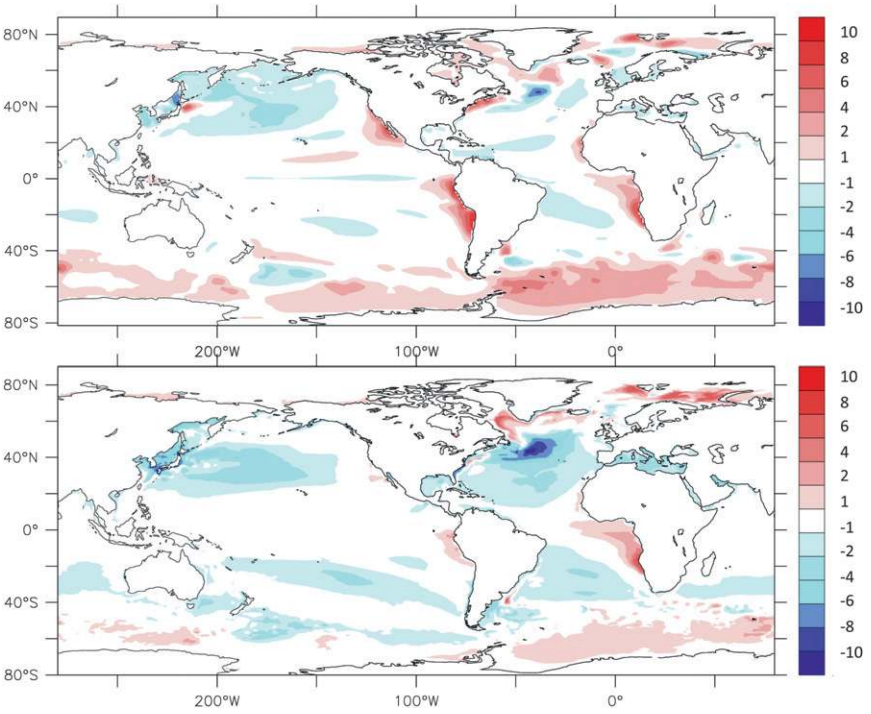

FIG. 2. Maps of errors in simulation of annual mean SST for (top) CM2.1 and (bottom) CM2.5. Units are K. The errors are computed as model minus observations, where the observations are from the Reynolds SST data (provided by the NOAA Cooperative Institute for Research in Environmental Sciences Climate Diagnostics Center; http://www.cdc.noaa.gov/). For the models, the annual mean, time-mean over years 101–200 of the 1990 control simulations are used. Note the nonlinear contour interval, and that there is no shading for values between −1 and +1 K. Positive values indicate the model is warmer than observations.

below, part of this initial cooling appears to be related to a model bias in which heat is pumped from the near-surface ocean layers into the interior ocean. The movement of heat away from the ocean surface leads to surface cooling, which is then amplified by cloud feedback; the cooler surface waters increase low-level cloudiness, resulting in the increased reflection of shortwave radiation to space and further cooling. On somewhat longer time scales there is a slow warming trend, related to the positive radiative imbalance and the overall warming of the ocean.

Shown in Fig. 2 are the maps of SST bias, computed as the annual mean simulated SST over years 101–200 of the 1990 control simulations minus that observed [positive values indicate that the simulated SST is larger than that observed; the observed data are described in Smith et al. (2008)]. The overall pattern of bias is similar between the two models, although the global mean temperature in CM2.5 is lower than in CM2.1, and this is reflected in Fig. 2 as well. A prominent bias remains in the simulation of the North Atlantic Current east of Newfoundland, with a large cold bias in both models, but the larger bias in CM2.5. This is a region of very sharp gradients in SST, so that small biases in the paths of ocean currents can lead to large SST biases. The warm bias in the Southern Ocean is reduced in CM2.5. One notable improvement in CM2.5 relative to CM2.1 is the near elimination of the positive SST biases off the west coast of South America and the southwest coast of North America. However, the overall root-mean-square error (RMSE) of simulated SST is similar between the two models (1.17 K in CM2.1 and 1.25 K in CM2.5).

Drifts in the ocean interior are shown in Fig. 3. In both models a cold bias develops in the upper 200 m, with a warm bias below that and a maximum warm bias around the 500–900-m depth. The overall warming signal is consistent with a positive radiative imbalance at the top of the atmosphere, with the net heat gained in the climate system being stored in the ocean interior. An important difference is that both the subsurface warming and the near-surface cooling are much larger in CM2.5 than in CM2.1; this aspect is discussed below.

The pattern of subsurface warming has maxima in the regions of the subtropical gyres (not shown), at depths from 500 to 900 m. This suggests that the warming drift may be related to subduction associated with the subtropical gyres.

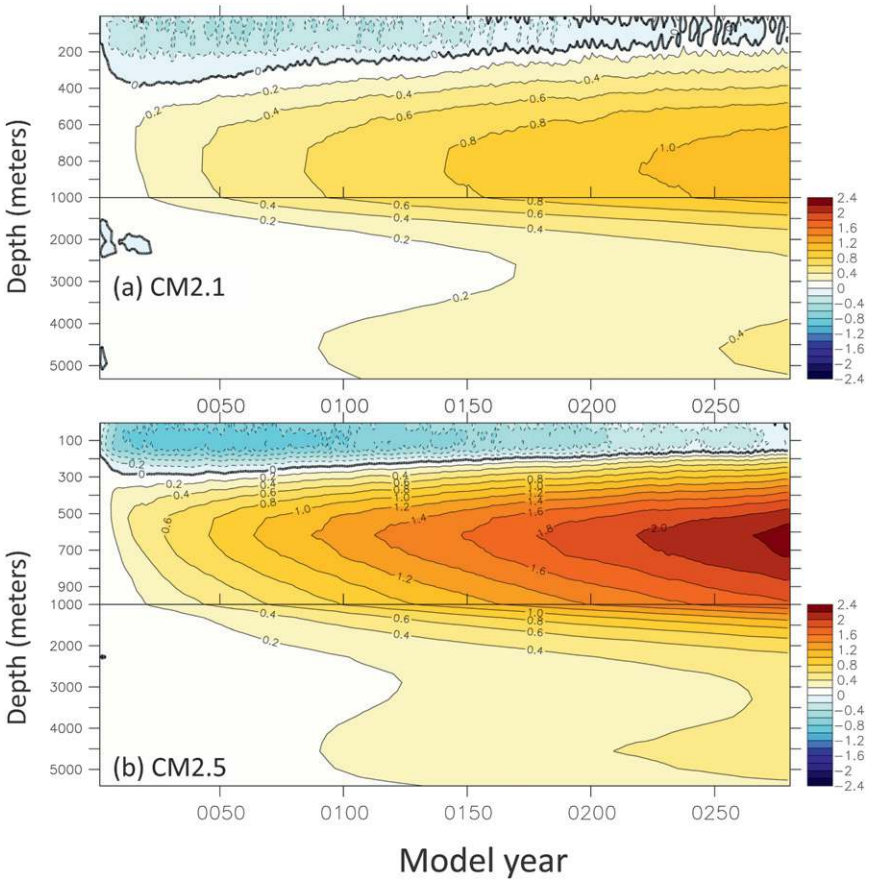

FIG. 3. Subsurface ocean temperature drift from initial conditions for (a) CM2.1 and (b) CM2.5. The values plotted are the differences between the global mean, annual mean temperature at each year minus the global mean, annual mean value at year 1. Units are K. Positive (negative) values indicate the subsurface ocean has warmed (cooled). Note the difference in the vertical scales above and below 1000 m.

A hypothesis for this drift is as follows: once the simulation starts, wind-driven subduction in the subtropical gyres deepens the thermocline, leading to the subsurface warming; this continues until other processes are strong enough to balance that deepening. We hypothesize that lateral heat transport by ocean mesoscale eddies is an important part of this balance, and that insufficient transport by eddies allows the thermocline in the models to deepen more than observed in nature; this leads to the subsurface warming drift. As the subtropical gyres deepen, the increased horizontal gradients should enhance mesoscale eddy activity, thereby enhancing the lateral transport of heat away from the gyres and inhibiting further deepening of the gyres and the subsurface warming. We hypothesize that in the absence of sufficient eddy heat transport (whether through explicitly resolved eddies or a parameterization of their effects), the thermocline in the subtropical gyres continues to deepen, implying continued movement of heat from the near-surface layers to the interior thermocline; this will result in the cool bias seen in the upper several hundred meters and the warm bias below.

The above hypothesis is consistent with the fact that the drift is larger in CM2.5 (which does not parameterize the effects of mesoscale eddies) than in CM2.1 (which includes such a parameterization). We test this hypothesis by conducting a simulation of CM2.1 that is identical to the 1990 control simulation described previously, but does not use a parameterization of mesoscale eddies. This new experiment is called CM2.1_1990_Control_NO_GM. The hypothesis predicts that the subsurface drift in this new experiment should be considerably larger than in the standard control run of CM2.1, since there are no eddy effects to inhibit the deepening of the subtropical gyres. Results (not shown) from this additional simulation support the hypothesis with the drift in the new run increased by almost a factor of 2. The largest increase in subsurface warm biases is in the subtropical gyres, also consistent with the hypothesis.

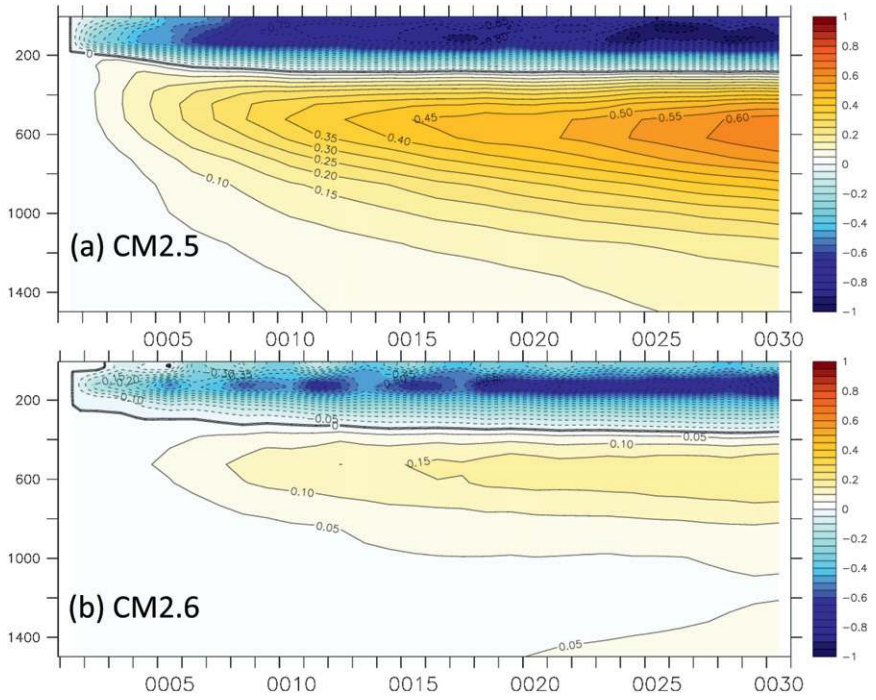

FIG. 4. Subsurface ocean temperature drift from initial conditions for (a) CM2.5 and (b) CM2.6. The values plotted are the differences between the global mean, annual mean temperature at each year minus the annual mean value at year 1. Positive (negative) values indicate the subsurface ocean has warmed (cooled). Units are K.

We can further test this hypothesis by using CM2.6, which has the same atmosphere as CM2.5 but uses a much finer resolution in the ocean. CM2.6 is computationally expensive to run, but we have conducted a 30-yr simulation using the same forcings as the 1990 control simulation of CM2.5, and using similar initial conditions as CM2.5. The above hypothesis predicts that CM2.6 should have a much smaller subsurface drift than CM2.5, since the much finer grid in CM2.6 will permit substantially enhanced eddy activity that should serve to moderate the deepening of the subtropical gyres. It will be shown later (see Fig. 14) that CM2.6 does indeed have much larger values of eddy kinetic energy (EKE) in the ocean, consistent with a much more vigorous mesoscale eddy field and closely resembling observational analyses. We show in Fig. 4 that when we have a very active eddy field, as in CM2.6, the subsurface drift is reduced by a factor of 3 or more relative to that in CM2.5. The near-surface cooling is also substantially reduced. This result using CM2.6 provides very strong support that the subsurface drift present in CM2.5 is largely attributable to insufficiently resolved mesoscale eddies in the ocean, combined with the lack of any parameterized eddy effects. This result is also a clear demonstration of the significant role that ocean mesoscale eddies may play in the climate system.

We note that biases in the surface winds can also impact the rate of subduction and this can also lead to subsurface biases. This was noted in Delworth et al. (2006) in a comparison of two versions of CM2 with differing atmospheric formulations and wind stress patterns. In that study, CM2.1 had considerably smaller subsurface drift in the South Pacific than CM2.0, and this was attributed to a significantly more realistic simulation of wind stress over the South Pacific in CM2.1 compared to CM2.0. However, since the atmospheric circulation is in general better in CM2.5 than CM2.1 (not shown), this does not appear to be a leading factor in causing the larger subsurface drift in CM2.5 relative to CM2.1.

b. Time-mean surface climate characteristics

We now wish to examine some of the time-mean simulation characteristics from the CM2.5 1990 control simulation. As a first assessment, we use near-surface air temperature and precipitation as simulated by the model to construct maps of Koppen climate classifications for both CM2.1 and CM2.5, and compare those to observations (see, e.g., Kottek et al. 2006; Gnanadesikan and Stouffer 2006). The Koppen climate classification system uses the seasonal cycles of temperature and rainfall at a continental location to characterize that location as belonging to one of a set of previously defined climatic

types. These include classifications such as tropical rain forest, savanna, desert, and polar. We calculate the percentage of continental areas in which the simulated Koppen climate classification type is different than observed. For CM2.1 this number is 23%, whereas for CM2.5 this number is 17%, a reduction in relative error of 26%. While there are widespread improvements, the largest improvements come from South America, where CM2.5 simulates substantially more rainfall over the Amazon basin. This demonstrates the substantial improvement of mean continental climate in terms of the seasonal cycles of temperature and precipitation for CM2.5 versus CM2.1.

We next examine precipitation as simulated over several continental regions. Shown in Fig. 5 is annual mean precipitation over North America from CM2.1, CM2.5, and a land-only observational dataset (Legates and Willmott 1990; updated data available at http://climate.geog.udel.edu/~climate/html_pages/precip_clim.html). There is a marked improvement in CM2.5 relative to CM2.1. Much of this improvement is likely attributable to the refined representation of orography in CM2.5, particularly over the western United States. For example, the precipitation maximum associated with the Sierra Nevada becomes apparent in CM2.5. However, there is generally too much rainfall over the western United States in CM2.5 compared to observations. The observed structure of the east–west gradient of precipitation over the Midwest is also more apparent in CM2.5, although the gradient is not as sharp as in the observations.

Shown in Fig. 6 is annual mean precipitation over Europe from observations (Legates and Willmott 1990), CM2.1, and CM2.5. Similar to North America, there is a significant improvement in precipitation in CM2.5 relative to CM2.1, likely associated with refined orography. For example, the structure of simulated precipitation over the United Kingdom is much improved in CM2.5 relative to CM2.1, with local maxima along the west coasts of Scotland and Ireland as in the observations. Similar improvements are clear over many other regions, including the coast of Norway and the Iberian Peninsula.

Shown in Fig. 7 is precipitation over India and the surrounding regions for the months of June–September (the monsoon season). We show results from two observational datasets [the satellite-based Tropical Rainfall Measuring Mission (TRMM) dataset and a station-based dataset] to provide a perspective on observational uncertainty in precipitation estimates in this region. CM2.5 shows notable improvement in simulated precipitation relative to CM2.1, a model which was found to have realistic simulations of South Asian monsoonal climate relative to the IPCC AR4 models (e.g., Annamalai et al. 2007; Rajeevan and Nanjundiah 2009). In particular, the two separate maxima in precipitation (one in the Western Ghats along the west coast, the other in the Gangetic Plain to the northeast) are captured realistically, as is the arid region in southern India and just off the southeast coast, although not as intense as observed. The structure of the rainfall maximum over the Bay of Bengal is improved, with more rainfall in the eastern portion of the bay, but the amount is still substantially less than observed. These results suggest that going to even finer resolution could yield further improvements.

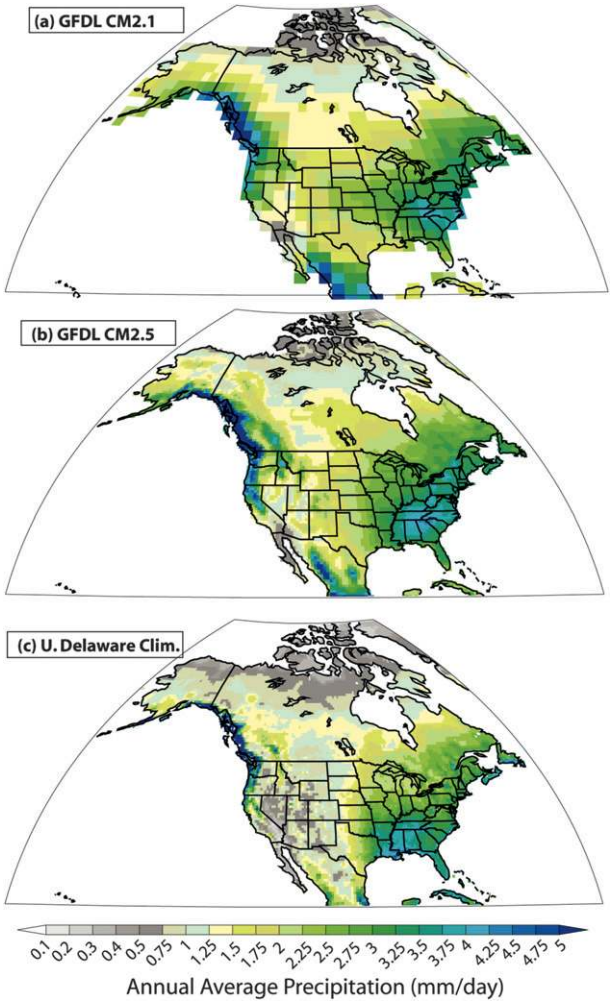

FIG. 5. Annual mean precipitation over land areas (mm day^{-1}) for (a) CM2.1, (b) CM2.5 and (c) observed data from University of Delaware (Legates and Willmott 1990; updated data available at http://climate.geog.udel.edu/~climate/html_pages/precip_clim.html). For model output, annual means from years 101–200 of the 1990 control simulations are used. Note the nonlinear contour scale.

Zonally averaged rainfall over the eastern tropical Pacific is shown in Fig. 8. The tendency for a double intertropical convergence zone (ITCZ) in CM2.1 is reduced in CM2.5, and the position of the rainfall maximum to the north of the equator is in better agreement

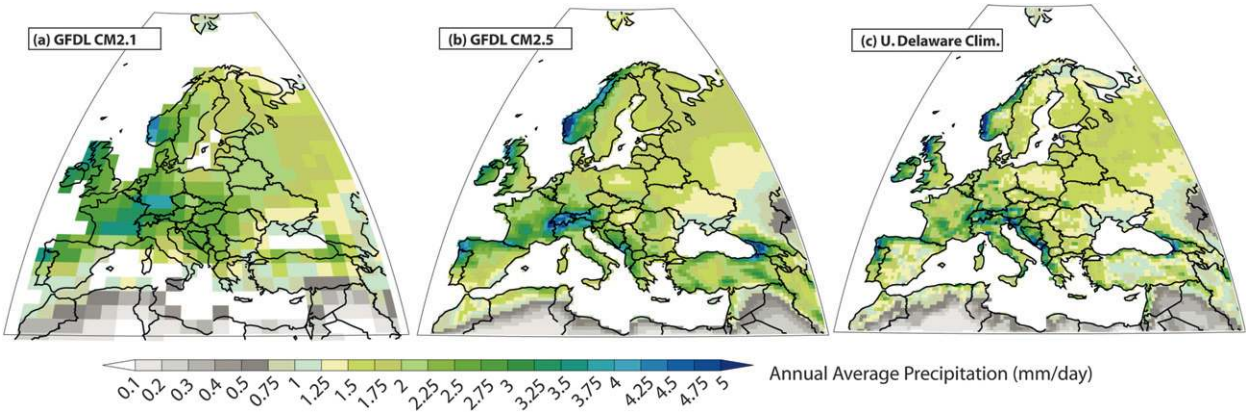

FIG. 6. Annual mean precipitation (mm day^{-1}) for (a) CM2.1, (b) CM2.5, and (c) observed data (Legates and Willmott 1990). For model output, time-mean, annual mean data from years 101–200 of the 1990 control simulations are used.

with observations. These improvements are also visible in Fig. 9, which shows maps of simulated and observed tropical rainfall. Rainfall in the eastern Pacific is reduced south of the equator in CM2.5, bringing CM2.5 in closer agreement with observations. There is an overall tendency for rainfall over the oceans to be more intense than observed. Rainfall over the Amazon improves significantly in CM2.5 relative to CM2.1, although it is still smaller than observed, and the rainfall maximum does not extend into southeastern Brazil as observed. The improved land model employed in CM2.5 may have helped in the simulation of Amazonian rainfall. The simulated South Pacific convergence zone is still more zonal in character than in the observations.

A factor contributing to the overall improvement of tropical precipitation, especially in the eastern Pacific, appears to be an improved representation of the Andes Mountains in South America and regional wind stress patterns, as well as small-scale oceanic features, including upwelling off the west coast of South America. Shown in Fig. 10 are maps of SST and the vertical structure of ocean temperature in this region from CM2.1, CM2.5, and an observational dataset (Antonov et al. 1998). It is clear that the coarse-resolution model (CM2.1) does not simulate the cool ocean temperature adjacent to the coast of South America between 5° and 20°S, whereas CM2.5 appears to capture this feature and bears a closer resemblance to the observations (cf. Figs. 10a–c). The cross sections of ocean temperature (Figs. 10d–f) demonstrate that relatively cool subsurface waters reach the surface in the observations and CM2.5, but not in CM2.1. There is a warm layer of near-surface water in CM2.1 close to the coast. These results suggest (and additional analyses, not shown, confirm) that coastal upwelling in CM2.5 is more vigorous, bringing cooler subsurface waters to the surface, resulting in the cool surface waters near the coast (see also Gent et al. 2010). This process appears to have a larger-scale influence, as the cool surface waters move northwestward with the mean surface currents, thereby cooling the surface water to the south of the equator in the eastern tropical Pacific. This distribution of SST tends to favor a single ITCZ north of the equator, instead of the double ITCZ seen in CM2.1 where there is also warm water south of the equator. These improvements in the representation of small-scale processes then have influence on a much larger scale. It is clear that CM2.5 still has a double ITCZ, but it is improved relative to CM2.1. Additional experiments that changed atmospheric or oceanic resolution separately suggest that changes in both the atmosphere and ocean resolution contributed to the improved SST and ITCZ simulations. It should be noted that similar improvements in the SST field do not occur in the eastern tropical Atlantic, where positive SST biases still dominate in CM2.5.

c. *Atmospheric temperature and circulation*

The atmospheric component of CM2.5 has considerably finer resolution than CM2.1 (~50 km in CM2.5 versus 200 ~ 280 km in CM2.1). We might expect this to lead to improvements in atmospheric circulation and temperature, and we briefly examine these changes here. Shown in Fig. 11 are the annual mean, zonal mean temperatures from the National Centers for Environmental Prediction (NCEP)–NCAR reanalysis (Kalnay et al. 1996) and from the CM2.1 and CM2.5 simulations. The simulation of atmospheric temperature is considerably improved in CM2.5 versus CM2.1 by this measure. To quantify this we calculate the root-mean-square difference between the NCEP–NCAR reanalysis values and the CM2.1 and CM2.5 simulations. By this metric, the difference from the reanalysis is reduced by 37% going from CM2.1 to CM2.5. The broad region of negative

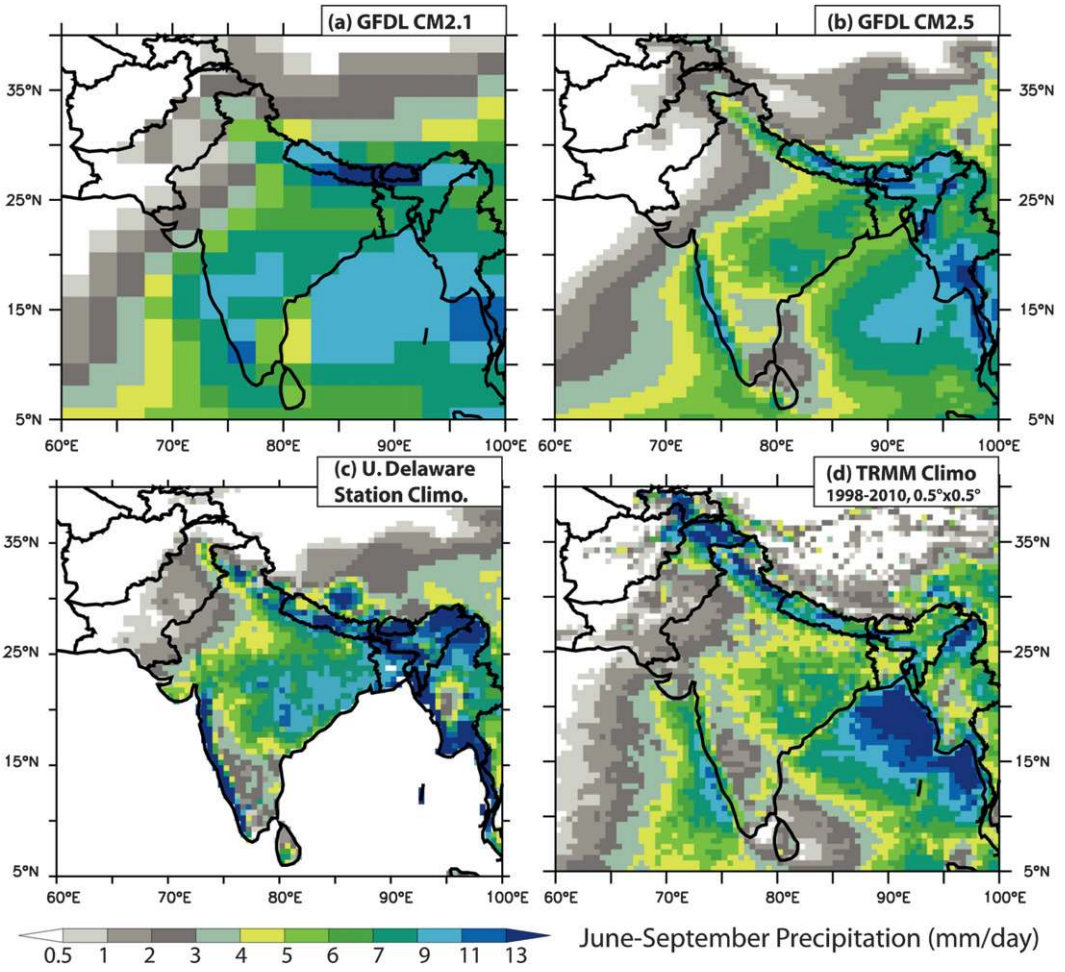

FIG. 7. Precipitation averaged over the months of June–September (mm day^{-1}) for (a) CM2.1, (b) CM2.5, (c) observed data over land areas from University of Delaware (Legates and Willmott 1990), and (d) observed data from TRMM satellite mission (TRMM-PR product 3A12: monthly 0.5° × 0.5° mean 2A12, profile, and surface rainfall downloaded from the National Aeronautics and Space Administration Mirador data server at http://mirador.gsfc.nasa.gov/). For model output, time-mean data from years 101–200 of the 1990 control simulations are used.

temperature anomalies in the upper troposphere in CM2.1 is considerably reduced in CM2.5. The positive temperature anomalies in the stratosphere in CM2.1 are also considerably reduced in CM2.5.

To examine the simulated stationary wave pattern, maps of the departures from the zonal mean of the 500-mb geopotential height field for NH winter [December–February (DJF)] were constructed and are shown in Fig. 12. By this metric, one of the largest atmospheric circulation deficiencies in CM2.1 is that the trough over northeastern North America in CM2.1 is much weaker than observed, leading to a zonal bias in the time-mean flow in that region. The simulation of this feature is considerably improved in CM2.5. More broadly, the pattern correlation between the CM2.1 stationary wave pattern and the NCEP–NCAR reanalysis is 0.90, and this improves to 0.97 in CM2.5. As an additional measure, the root-mean-square of the differences between CM2.5 and the NCEP reanalysis is 33% smaller than between CM2.1 and the NCEP reanalysis. These statistical measures quantify the visual impression of the improvements, and serve as one measure of the improved atmospheric circulation in CM2.5 relative to CM2.1. Future analyses will examine in more detail the changes in atmospheric simulations between CM2.1 and CM2.5, including storm tracks and other variability characteristics.

d. Large-scale ocean circulation characteristics

The ocean circulation is far more energetic in CM2.5 than in CM2.1. Shown in Fig. 13 are maps of the time-mean ocean surface velocities in CM2.1 and CM2.5 for parts of the North Atlantic. The finer resolution, lower

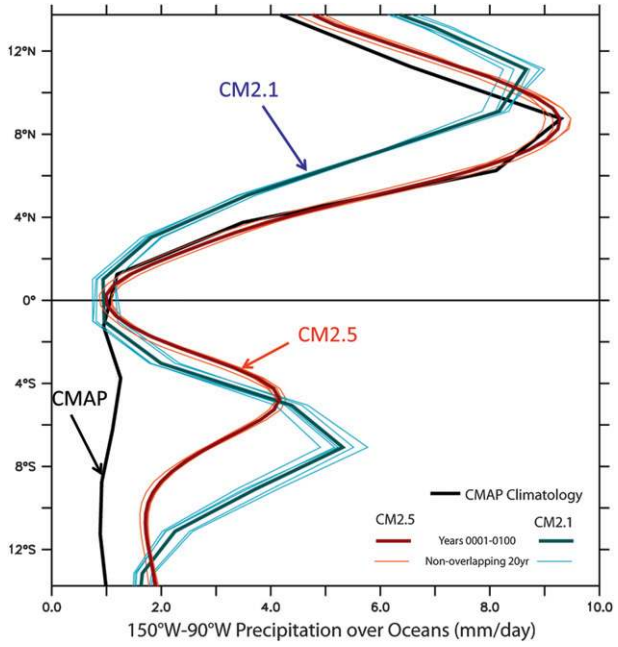

FIG. 8. Annual mean precipitation (mm day^{-1}). The thin red and blue lines show the distribution of the five separate 20-yr mean precipitation values over the period of years 101–200, while the thick red and blue lines show the 100-yr mean values. The clustering of the 20-yr means around the 100-yr means suggests the differences between CM2.1 and CM2.5 are robust. The Climate Prediction Center Merged Analysis of Precipitation (CMAP) data are described in Adler et al. (2003), and the Global Precipitation Climatology Project data are described in Xie and Arkin (1997).

viscosity, higher-order advection scheme, and lack of explicit lateral diffusion used in CM2.5 permit the model to simulate much higher velocities, especially in the vicinity of the boundary currents. For example, the largest annual mean northward current speed off the east coast of Florida is 1.42 m s^{-1} in CM2.5, compared to 0.37 m s^{-1} in CM2.1. The boundary currents also have much tighter and less diffusive structures. Compare, for example, the boundary flows around the periphery of the Labrador Sea in both models. Consistent with the tighter boundary currents are larger gradients of SST in CM2.5 than in CM2.1 (not shown), especially in the region of boundary currents such as the Gulf Stream and Kuroshio. Consistent with this (Minobe et al. 2008) and the finer atmospheric resolution, horizontal gradients of precipitation are also considerably increased in the vicinity of sharp SST gradients (not shown).

Shown in Fig. 14 are maps of the eddy kinetic energy in the models and derived from satellite observations. The map of EKE in observations (Fig. 14a) shows a rich structure, with large EKE in boundary currents and some interior regions. The coarse resolution of CM2.1 does not permit the formation of eddies, with the exception of the deep tropics, and the EKE amplitude in CM2.1 is thus very small (Fig. 14b). The EKE field is more realistic in CM2.5 (Fig. 14c) than in CM2.1, as to be expected from the finer resolution and lower viscosity. The magnitude of the EKE in CM2.5 is still, however, somewhat below that observed, suggesting that still finer ocean resolution is needed to fully capture eddy kinetic energy. This point is confirmed when examining EKE in CM2.6 (Fig. 14d), which is in excellent agreement with observational estimates.

The comparison of Figs. 14c,d shows that the resolution of CM2.5 is not adequate to fully resolve the effects of oceanic eddies in the climate system. While we have explored versions of CM2.5 that attempt to parameterize these effects, the current version of CM2.5 does not use such a parameterization. Our approach has been to use a comparison of CM2.5 and CM2.6 to explicitly evaluate the impact of oceanic mesoscale eddies, since CM2.6 successfully resolves these features and only differs from

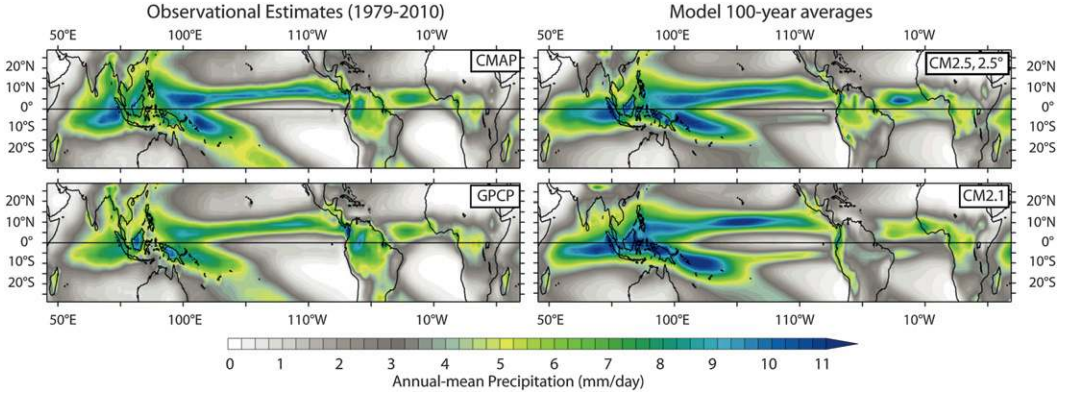

FIG. 9. Annual mean precipitation (mm day^{-1}). (left) Observational estimates with (top) CMAP and (bottom) GPCP. (right) Simulated precipitation with (top) CM2.5 and (bottom) CM2.1. Note that the CM2.5 results are plotted on a grid that is much coarser than its native model grid, but similar to that for CM2.1 and the observations.

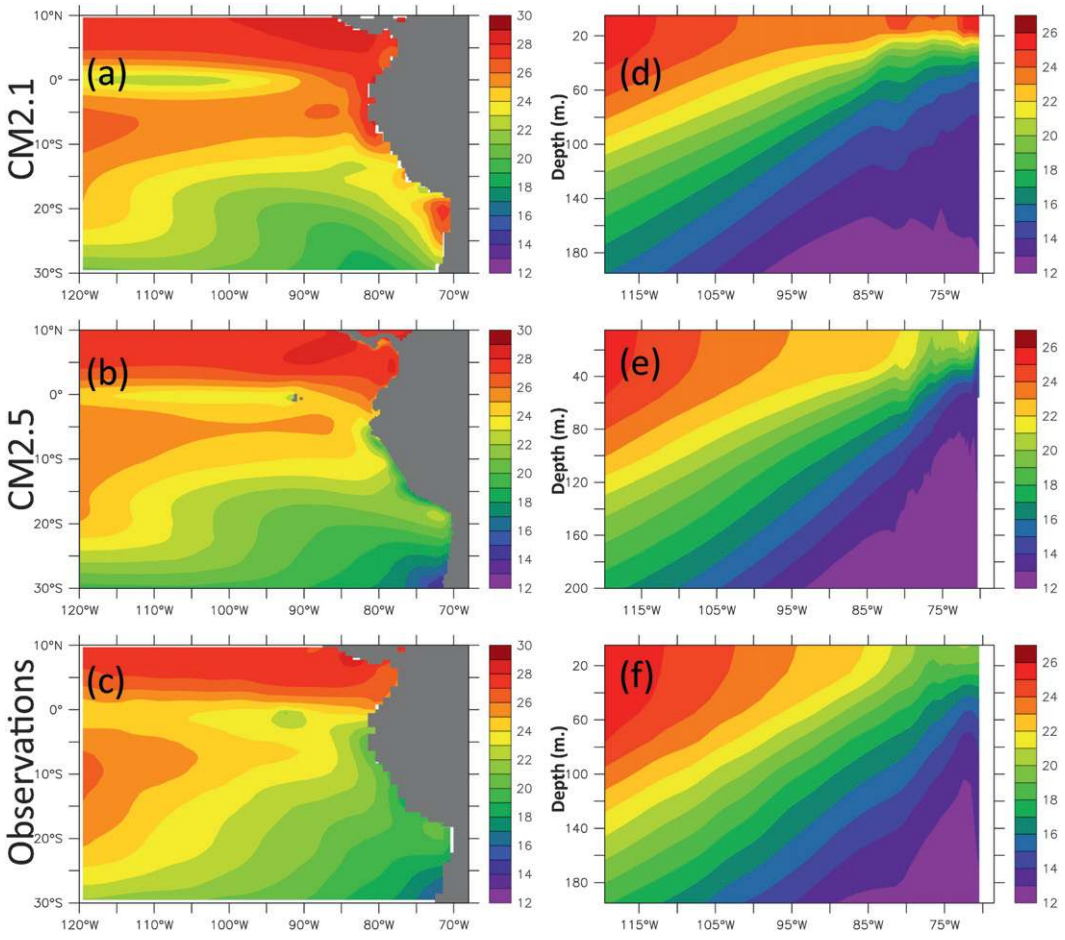

FIG. 10. SST (°C) from the control (a) CM2.1 and (b) CM2.5 calculated as annual mean over years 101–200. (c) Observed SST (Antonov et al. 1998). Cross section of annual mean temperature averaged over years 101–200, and averaged over latitudes 5°–20°S: data from control (d) CM2.1 , (e) CM2.5, and (f) observations (Antonov et al. 1998). The *y* axis is depth in m.

CM2.5 in terms of oceanic resolution. Future work with CM2.5 will further explore the incorporation of a parameterization of ocean mesoscale eddies.

The structure of the time-mean Atlantic meridional overturning circulation (AMOC) is shown in Fig. 15 for CM2.1 and CM2.5 (the definition of this field is described in the figure caption). The overall transport is reduced in CM2.5 relative to CM2.1. At 26.5°N, the AMOC in CM2.5 is 14.4 Sverdrups (Sv; 1 Sv = 10^6 m^3 s^{-1}) versus 18.1 Sv in CM2.1; the most recent observational estimate of the AMOC at 26.5°N is 18.5 Sv (Johns et al. 2011; Kanzow et al. 2010). The total poleward oceanic heat transport in the North Atlantic in CM2.5 peaks at about 10^{15} watts (1 PW), similar to CM2.1, but less than recent observational estimates of 1.3 PW (Johns et al. 2011).

We speculate that insufficiently resolved overflows of dense water through the Denmark Strait and Faroe channels may contribute to this somewhat weak North Atlantic heat transport. In a separate sensitivity test using CM2.5 with deepened topography downstream of the Denmark straits (see Zhang et al. 2011 for details), the outflow of dense water from the Nordic Seas was significantly enhanced, resulting in a deepening of the AMOC by about 1000 m. There was also an increase in the total oceanic heat transport in the North Atlantic from 0.96 to 1.13 PW at 26.5°N, and the AMOC at 26.5°N increased from 15 to 18 Sv. However, these results were based on 5-yr means from a short sensitivity test, and they need to be confirmed with additional sensitivity tests. They do suggest, however, that deficiencies in the representation of overflows may contribute to this bias. This issue is discussed further in section 4c below.

In the Southern Hemisphere, the Antarctic Circumpolar Current (ACC) is a major feature of the oceanic circulation in high latitudes. One measure of this flow, defined as the total zonal oceanic volume transport

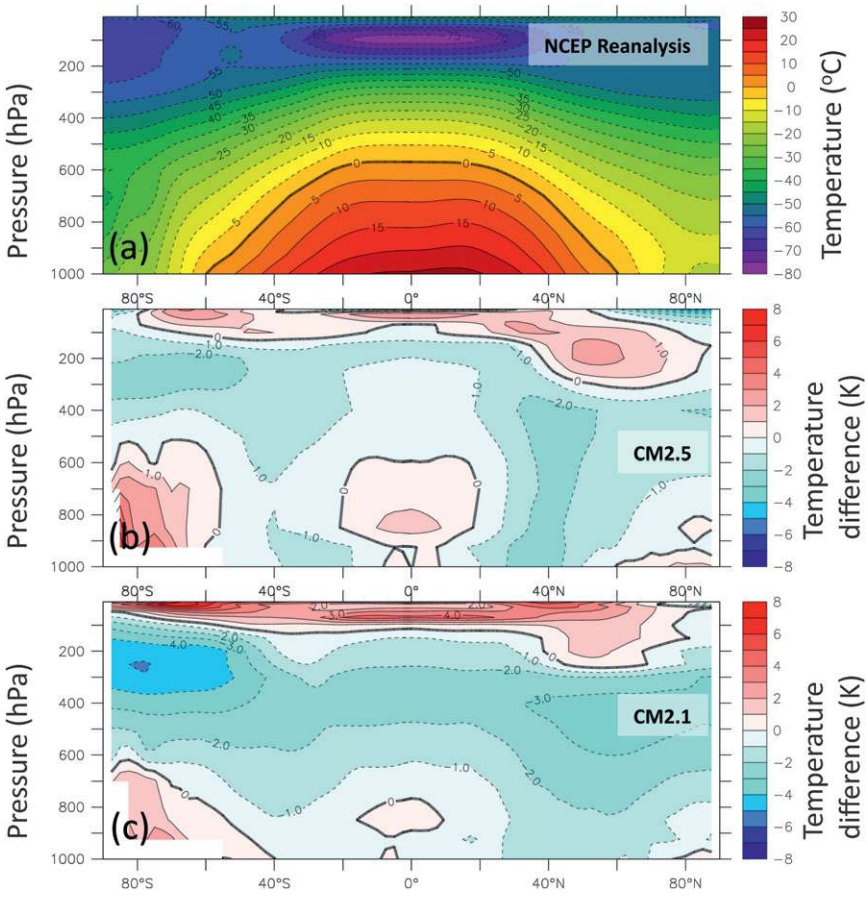

FIG. 11. (a) Zonal mean, annual mean air temperature (°C) from the NCEP–NCAR reanalysis averaged over the period 1958–97, plotted as a function of height. Zonal mean, annual mean air temperature from (b) CM2.5 and (c) CM2.1 minus the NCEP–NCAR reanalysis values. CM2.5 temperatures are the time mean from years 101–200 of the 1990 control simulation. Positive values indicate the model is warmer than the observations.

through 82°W between Antarctica and South America, from the surface to the bottom of the ocean has a time-mean value of 116 Sv in the CM2.5 control simulation. This is somewhat smaller than the value of 130–140 Sv found in CM2.1 (see Fig. 9 of D06), and smaller than observational estimates of 135 Sv (Cunningham et al. 2003), although the uncertainty associated with the observational estimates can be significant. After an initial weakening in the control simulation, the circulation is fairly steady, with modest variability (not shown).

e. Sea ice

There is a change in the simulation of annual mean sea ice thickness between CM2.1 and CM2.5, as shown in Figs. 16a,b. In the Arctic, the sea ice in CM2.5 is substantially thicker than in CM2.1, with maximum sea ice values near the Canadian and Greenland coasts. The increase in albedo between CM2.1 and CM2.5 (see section 2d) is a substantial contributor to the thicker (and more realistic) sea ice in CM2.5. Improved atmospheric circulation (not shown) also helps to create the drift stream of sea ice from Siberia to the Canadian archipelago. This feature is more diffuse in CM2.1. A similar improvement in sea ice relative to CM2.1 is also seen in GFDL CM3 (Griffies et al. 2011).

There is also an increase in sea ice thickness in the Southern Hemisphere (Figs. 16c,d), with very large values in small-scale bays and inlets (these are also seen in the Northern Hemisphere). As mentioned briefly in section 2d, the fine resolution allows the model to include many small bays and inlets. In such regions, the flow of snow and ice into the ocean is a complex process, including such factors as ice shelves and grounded ice sheets. The model is not able to satisfactorily represent such small-scale processes. One of the consequences is that sea ice can be formed in such restricted areas as snow builds up in continental regions and ''runs off'' (calves) into the small bays and inlets. However, the rate

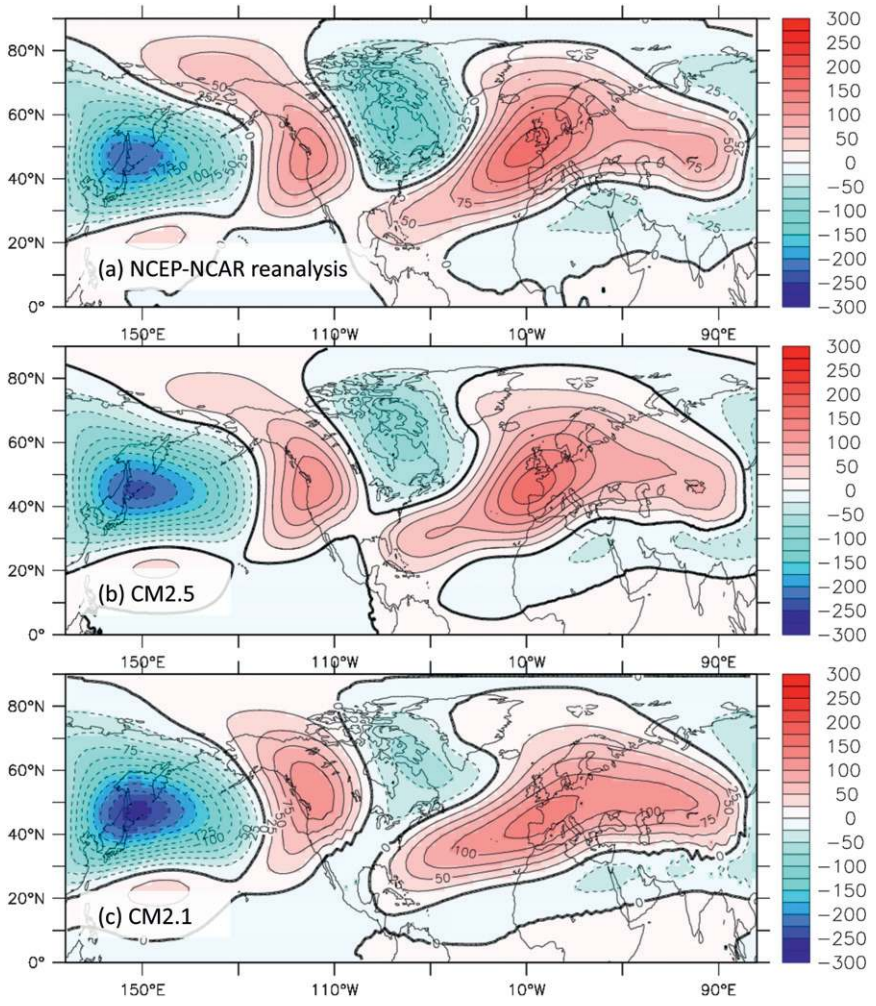

FIG. 12. (a) Geopotential height (m) at 500 hPa for DJF after removing the zonal mean. This represents the stationary eddy field. Data are from the NCEP–NCAR reanalysis, averaged over the period 1958–97. (b),(c) Same as (a) using output from CM2.5 and CM2.1, respectively, over years 101–200 of the 1990 control simulation. The pattern correlation between the CM2.1 results and the NCEP–NCAR reanalysis is 0.90; this value increases to 0.97 for the correlation between the CM2.5 results and the NCEP–NCAR reanalysis.

at which this new ice forms is sometimes greater than the rate at which the model is able to move such ice into the open ocean where it can melt. As a result, ice can grow unrealistically thick in such regions (to hundreds of meters). This points to a need for improved representation of such coastal ice processes in future high-resolution models. The problem is much less severe at coarser resolutions where the connection of coastal regions to the open ocean is less restricted.

f. ENSO

Previous work has described the tropical climate and ENSO in CM2.1 (Wittenberg et al. 2006; Wittenberg 2009; Kug et al. 2010). Here we focus on how CM2.5's tropical variability and ENSO compare with observations and CM2.1.

The spatial patterns of tropical interannual SST variability are shown in Fig. 17 [observations from Smith et al. (2008); model diagnostics of ENSO-related variability in Figs. 17–19 use the full length of the experiments]. CM2.1_1990 exhibits strong equatorial Pacific variability (ENSO), stronger than that observed in recent decades. Both CM2.1_1990 and CM2.5_1990 place the center of Pacific sea surface temperature anomaly (SSTA) variability west of the observed pattern, with too little variability along the coast of Peru; both are common biases among coupled general circulation models (CGCMs; Guilyardi et al. 2009). However, CM2.5 agrees more

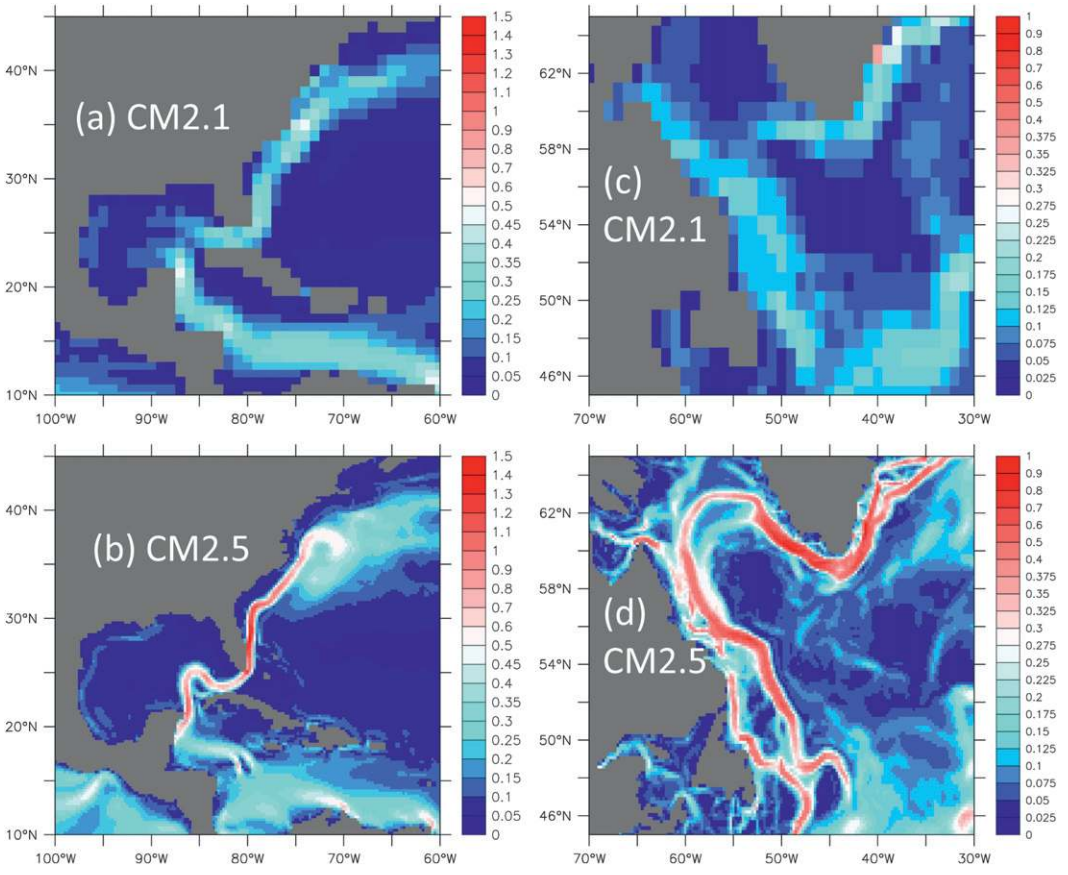

FIG. 13. Annual mean surface current speed (m s^{-1}). Gulf Stream region for (a) CM2.1 and (b) CM2.5. Labrador Sea region for (c) CM2.1 and (d) CM2.5. All values plotted are annual mean averages over the period of years 101–200 of the 1990 control runs.

closely with observations than CM2.1, with a weaker Pacific ENSO (especially west of the date line) and weaker interannual variability of Indian Ocean SSTs. Within the tropics, only the Atlantic shows stronger interannual SSTA fluctuations in CM2.5 than in CM2.1. With CO_2 doubling, both models show a slight increase in tropical interannual SST variability (not shown).

Figure 18 shows time-mean spectra of Niño-3 SSTs for the models and observations. All three time series exhibit interdecadal modulation of the ENSO amplitude and period, producing a broad spectrum in the interannual band. The interdecadal modulation of ENSO poses challenges for evaluating models using short observational records, and for assessing the future of ENSO (Wittenberg 2009; Vecchi and Wittenberg 2010; Collins et al. 2010). Yet it is clear that the CM2.1 spectrum is stronger than observed at semiannual and interannual time scales—a difference detectable even with time series as short as 20 yr. In comparison with CM2.1, the CM2.5 spectral power is generally weaker and more consistent with observations, except at periods near 2–2.5 yr where the CM2.5 spectrum peaks.

The seasonal cycle of tropical SST has weakened slightly in CM2.5 relative to CM2.1, which represents an improvement relative to observations. The largest attenuation is near the coast of Peru, where both the SST and southeasterly wind seasonal cycles have weakened in CM2.5 (not shown). The cause may be CM2.5's weaker upper-ocean thermal stratification near South America, as seasonal wind anomalies and their associated upwelling (linked to the seasonal migration of the ITCZs) tap into a weaker subsurface contrast and thereby generate weaker seasonal SST changes. The reduced seasonally alternating ITCZ in CM2.5's eastern tropical Pacific, and associated reductions in the semiannual cycle of equatorial wind speed and evaporation, have also weakened the semiannual cycle of Niño-3 SST, again bringing CM2.5 more in line with observations.

In observations, the Niño-3.4 SSTA warm events generally peak in October–December and the cold events peak in October–January. As discussed in Wittenberg et al. (2006), CM2.1 warm and cold events exhibit less seasonal phase locking than observed; they can peak any

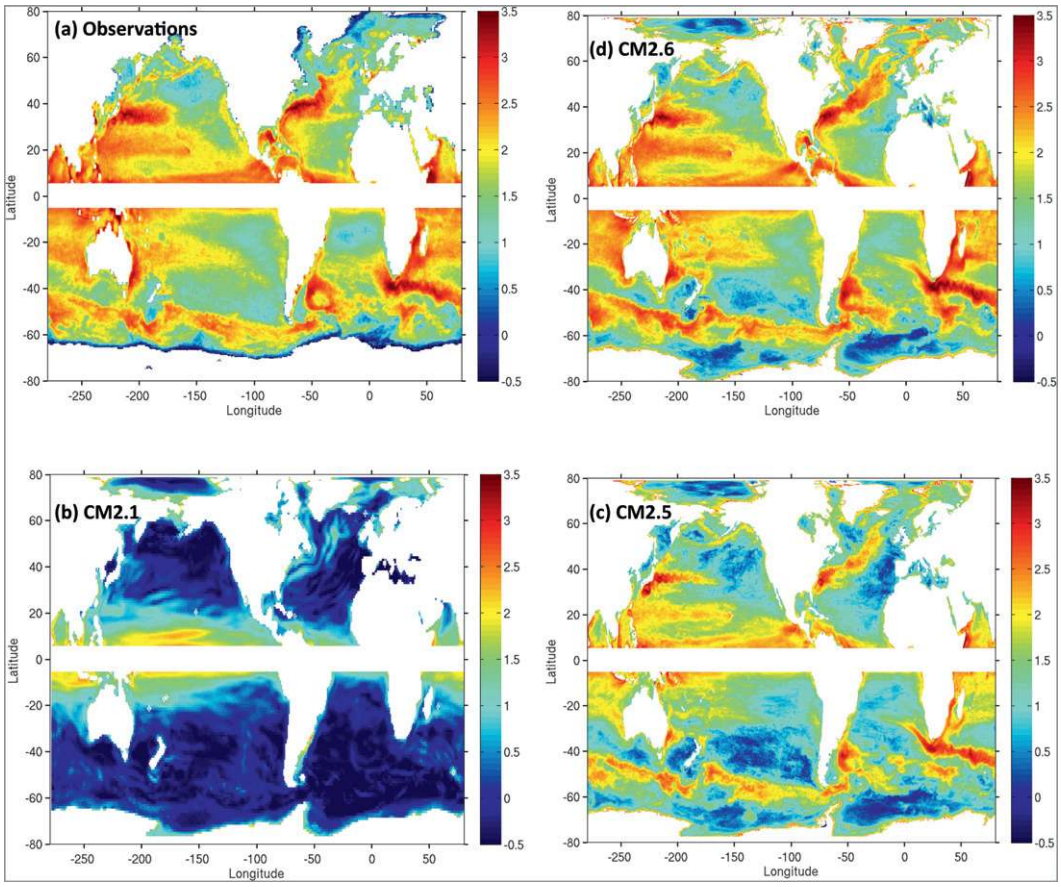

FIG. 14. Maps of the logarithm of EKE ($cm^2\ s^{-2}$) for (a) observations, (b) CM2.1, (c) CM2.5, and (d) CM2.6. In these calculations we start from sea surface height, available directly from the model simulations, and from satellite altimetry in the observations (Le Traon et al. 1998). Instantaneous values taken every 7 days are used. The period 2002–06 is used for the observations, and years 6–10 for the models. The sea surface heights are used to compute near-surface currents using geostrophy. Eddy velocities are computed as deviations from the long-term mean, from which EKE is then calculated and plotted on a logarithmic scale. No values are plotted within 5° of the equator, since the geostrophic approximation is not fully valid there.

time of year, with Niño-3.4 warm events peaking slightly more often between October and February. Additional analyses (not shown) indicate that the Niño-3.4 phase locking is somewhat improved in CM2.5, with an enhanced tendency for warm events to peak in December and for cold events to peak in December–January; however, the locking remains weaker and later than observed. In the Niño-3 region, which sits slightly farther east, the event histogram in CM2.5 (not shown) actually displays semiannual peaks (as did CM2.1), with warm events peaking any time of year but preferentially in July–August or January–February, and cold events in August–September or January–February. This is quite unlike the observations, which exhibit a clear locking of warm events to the end of the calendar year in both Niño-3.4 and Niño-3. The semiannual locking of Niño-3 SSTAs in CM2.1 and CM2.5 may arise from the unrealistic north–south alternation of the ITCZ about the equator in the eastern Pacific in both simulations, which produces a seasonal reversal of the meridional winds and an associated semiannual cycle in evaporation, rainfall, and currents near the equator. Despite the improved tropical Pacific climatology in CM2.5, it may be that CM2.5's (realistically) weaker ENSO events remain unable to produce sufficient SSTAs in the eastern Pacific to interact strongly with the seasonal cycle of convection, resulting in weaker ENSO phase locking than observed.

The shorter ENSO period in CM2.5 may be linked to a change in the structure of the wind stress response to SSTAs (not shown). Compared to CM2.1, in CM2.5 the equatorial westerly wind stress anomalies that develop near the date line during warm events are meridionally narrower and more trapped in the west, especially on their southern flank. Studies have shown that models

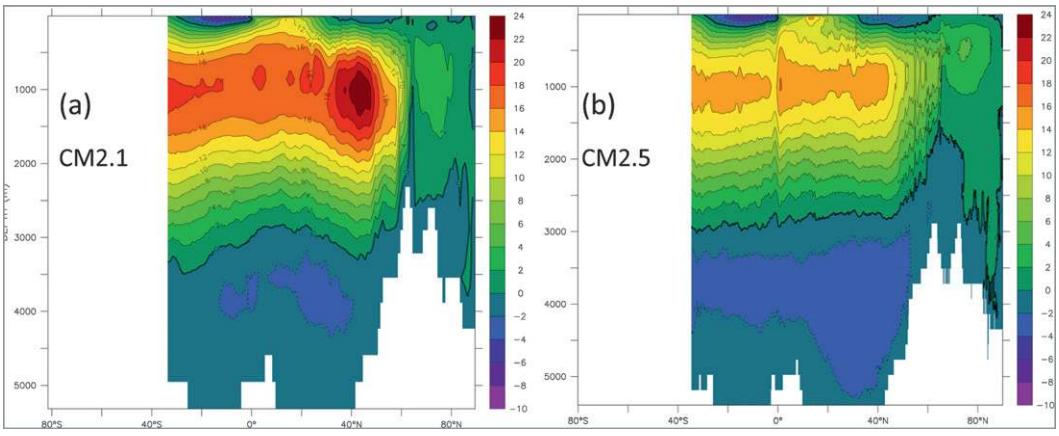

FIG. 15. Spatial pattern of the AMOC in (a) CM2.1 and (b) CM2.5. This field is computed as the definite integral of the meridional volume transport across the North Atlantic, and the indefinite integral from the ocean bottom to the surface. Units are Sv. Flow is clockwise around a maximum value in the depth–latitude plane Calculations are performed using annual mean, time-mean data for years 101–200 of the 1990 control simulation.

with narrower or westward-shifted westerly anomalies tend to exhibit weaker ENSOs with shorter periods (Kirtman 1997; An and Wang 2000; Wittenberg 2002; Capotondi et al. 2006; Kim et al. 2008). This change occurs because of the increased cyclonic wind stress curl close to the equator and western boundary during warm events, which shortens the time needed for the off-equatorial oceanic Rossby wave train to reflect at the

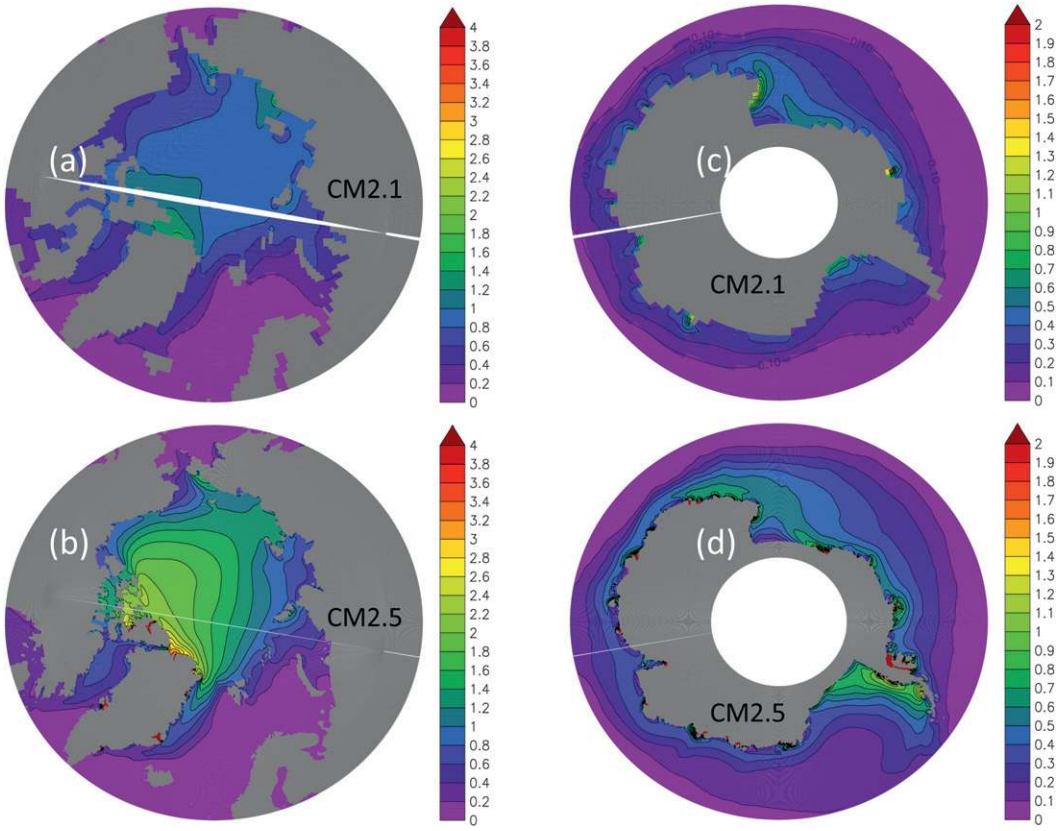

FIG. 16. Annual mean sea ice thickness (m) for (a) CM2.1, NH, (b) CM2.5, NH, (c) CM2.1, SH, and (d) CM2.5, SH. Note that there are different shading levels for the NH and SH.

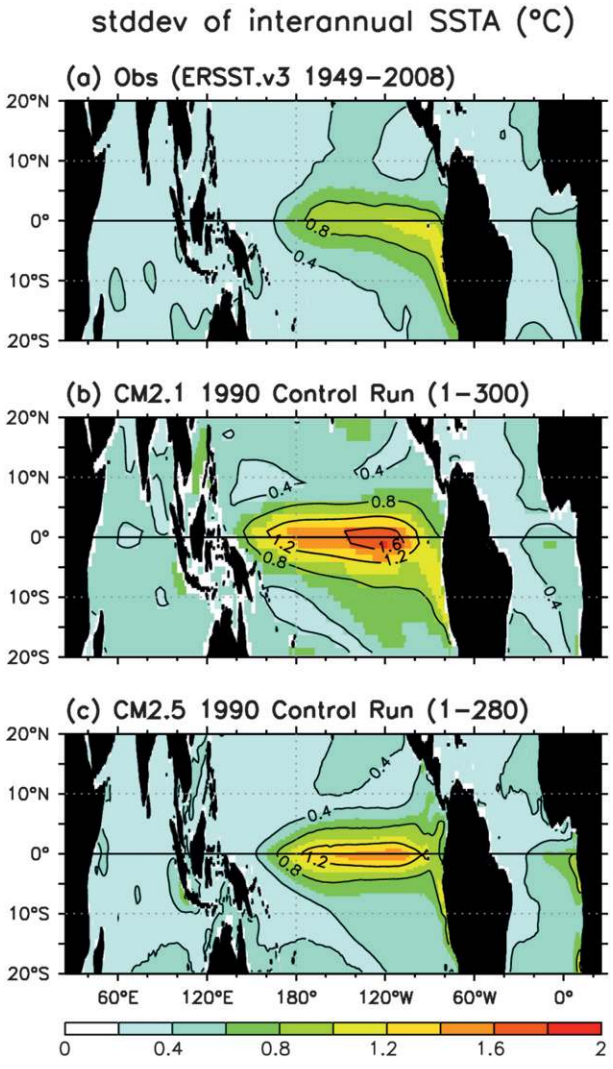

FIG. 17. Standard deviation of SST anomalies (°C) over the tropics, after applying a 9-month triangle smoother that transmits (25, 50, and 75)% of the time series amplitude at periods of (8, 11, and 17) months. (a) Observations from Smith et al. (2008), years 1949–2008, (b) CM2.1 1990 control run, years 1–300, and (c) CM2.5 1990 control run, years 1–280. Note that in contrast to many of the other analyses in this paper, the full length of the model experiments to characterize ENSO-related variability is used.

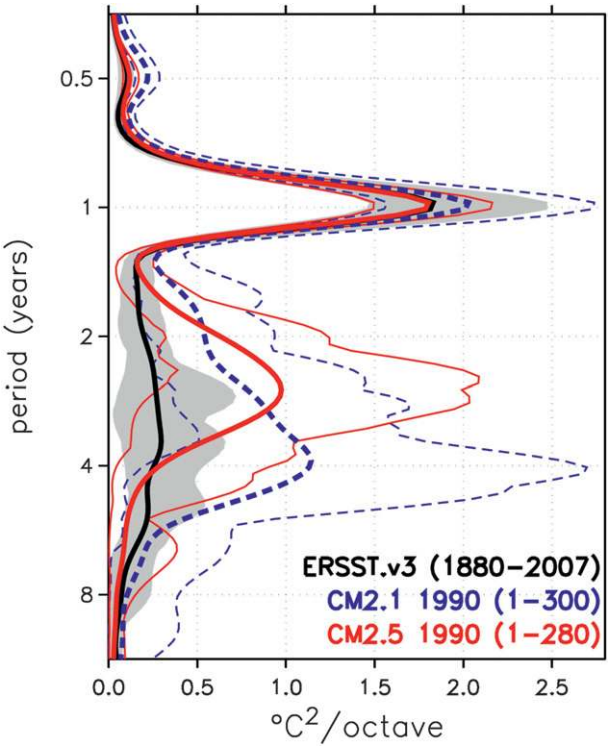

FIG. 18. Spectral power ($°C^2$ $octave^{-1}$) of Niño-3 SSTs, as a function of period in octaves of the annual cycle, computed by time averaging the spectral power density from a Morlet wavenumber-6 wavelet analysis. The area to the left of each curve represents the spectral power within a frequency band. Thick black line is the observed 128-yr-mean spectrum for 1880–2007, from the NOAA Extended Reconstructed Sea Surface Temperature, version 3 (ERSST.v3) (Smith et al. 2008). Thick blue dashed (red solid) line is the 300-yr-mean (280-yr mean) spectrum from years 1–300 (1–280) of the CM2.1 (CM2.5) 1990 control run. Gray shading (thin lines) indicates the min/max range of sliding 20-yr-mean spectra from the observed (simulated) time series.

western boundary as equatorial Kelvin waves. This shorter time for wave reflection more rapidly reverses the sense of zonal advection along the equator, and also more rapidly establishes a poleward Sverdrup transport that discharges upper-ocean heat content from the equator. Both effects contribute to a faster termination of warm events in models with meridionally narrower or westward-shifted Pacific zonal wind stress anomalies. The narrower zonal wind stress anomalies in CM2.5 may themselves result from the meridionally narrower rainfall anomalies in that model, linked to the equatorward-shifted climatological ITCZs (see Fig. 8).

Another factor behind the attenuation of ENSO in CM2.5 versus CM2.1 is stronger damping of SSTAs by surface heat fluxes in CM2.5 (not shown). For CM2.5 warm events, there is a larger cloud-shading response in the central Pacific (as deep convection shifts farther east than in CM2.1), and also in the east Pacific (as ITCZ deep convection shifts farther equatorward than in CM2.1). In CM2.5 there is also more evaporative cooling during warm events. This increased cooling is due to higher SSTs and drier surface air in the mean state, which make evaporation more sensitive to SSTAs than in CM2.1, and also to more anomalous warming of SST and drying of surface air in the eastern equatorial Pacific during CM2.5's warm events, which further increases the evaporative damping of SSTAs.

Figure 19 shows the boreal winter response of northern extratropical circulation to ENSO. As described in

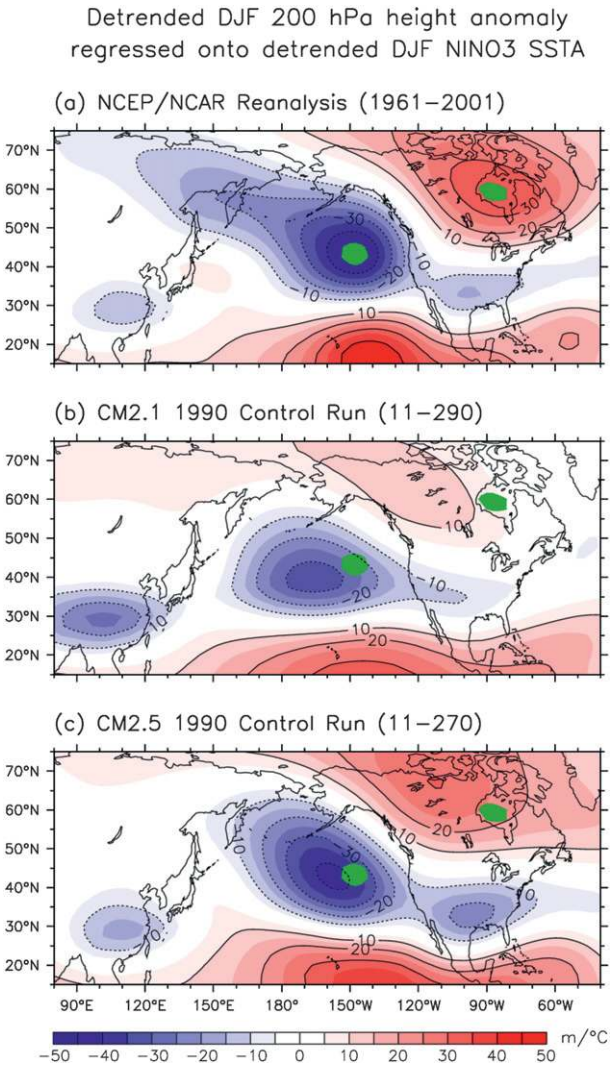

FIG. 19. DJF 200-hPa geopotential height anomalies regressed onto DJF Niño-3 SSTAs, computed using (a) the NCEP–NCAR reanalysis (Kistler et al. 2001) for 1961–2001, (b) the CM2.1 1990 control run for years 11–290, and (c) the CM2.5 1990 control run for years 11–270. The zero contour is omitted. Green shading indicates the positions of the observed extrema over the North Pacific and Canada. Prior to computing the seasonal anomalies and regressions, all time series were detrended by removing a 20-yr running mean.

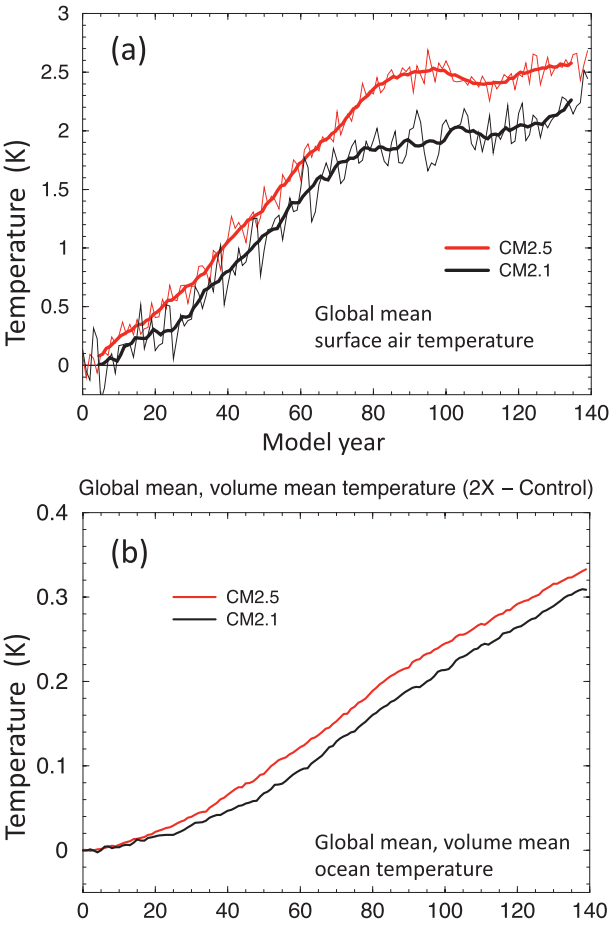

FIG. 20. (a) Time series of response of global mean near-surface air temperature to increasing atmospheric CO_2. Annual mean temperature responses are plotted, calculated as temperature from the $2X\_CO_2$ runs minus the temperature from a corresponding section of the control runs. Thin lines indicate annual means (black for CM2.1, red for CM2.5), while thick lines indicate 10-yr low-pass filtered time series (black for CM2.1, red for CM2.5). (b) Global mean, volume mean ocean temperature change, $2X\_CO_2$ experiment minus control. Black curve for CM2.1, red curve for CM2.5.

Wittenberg et al. (2006), CM2.1 exhibits 200-hPa geopotential height extrema that are weaker than and displaced 20°–30° west of those observed—due in part to similarly westward-shifted responses of the equatorial SST and rainfall. While the North Pacific low and Canadian high remain displaced somewhat westward from their observed positions in CM2.5, there are also significant improvements in the extratropical response. The extrema over the North Pacific and Canada have strengthened, the Pacific low extends farther northwestward toward Siberia, the low over the southeastern United States has become a distinct center, and the low over southeastern China has weakened.

4. Response to increasing CO_2

We next assess the sensitivity of CM2.1 and CM2.5 to increasing CO_2. As described in section 2f, we have completed simulations in which CO_2 increases at a rate of 1% yr^{-1} until reaching double its initial concentration after 70 yr; and is then held constant for the remaining 70 yr of the simulation. The complete climate system, especially the deep ocean, will not come into equilibrium over this time scale, and so we are examining

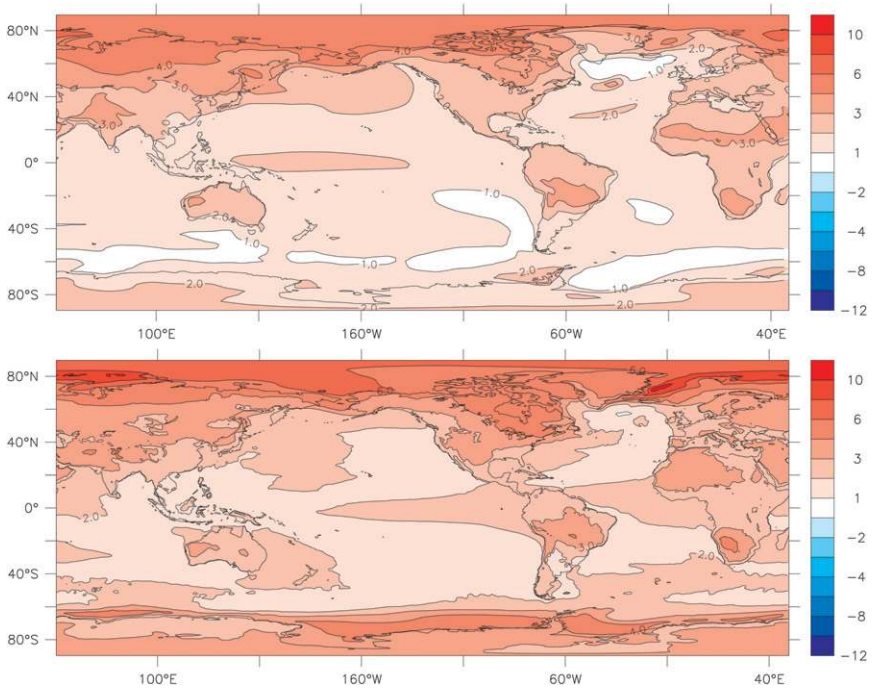

FIG. 21. Map of change in annual mean near-surface air temperature in response to increasing CO_2 for (top) CM2.1 and (bottom) CM2.5. Maps are computed using data averaged over years 91–140 of the 2X_CO_2 runs minus the corresponding sections of the control runs. Units are K.

aspects of the transient response. Note that as described in section 2f we use a slightly modified version of CM2.1 for the 2X_CO_2 simulations, and this can be referred to as CM2.1v2. However, since the simulations of CM2.1 and CM2.1v2 are extremely similar, and their responses to increasing CO_2 are also similar, for convenience we shall still refer to this slightly revised version of the model as CM2.1. The essential conclusions as described are similar for CM2.1v2 and CM2.1 (as evaluated from a 2X_CO_2 simulation starting from an 1860 control simulation).

a. Transient response

Shown in Fig. 20a are the time series of global mean, annual mean near-surface air temperature changes in response to increasing CO_2. The response is computed as the simulated values in the 2X_CO_2 experiments minus corresponding values from the control simulations. It is clear that both the rate of warming and the total warming in CM2.5 are somewhat larger than in CM2.1. Since the atmosphere–land component of CM2.5 differs somewhat from CM2.1, especially with regard to the land model used, it is not clear to what extent the different response reflects different physics versus different resolution. Shown in Fig. 20b are time series of global mean, volume mean ocean temperature changes in response to increasing CO_2. The oceanic rate of heat uptake in CM2.5 is slightly larger than in CM2.1 for the first 70 yr, but appears similar thereafter. Thus, both the ocean and the near-surface atmosphere are warming somewhat more rapidly in CM2.5 than in CM2.1 for the first 70 yr. The transient climate response (global mean temperature change at the time of CO_2 doubling) is approximately 1.6 K in this version of CM2.1 and 2.0 K in CM2.5. Further work will be necessary to evaluate whether the higher resolution in CM2.5, especially in the ocean where eddies may have important effects, plays any role in the differing response to CO_2.

b. Patterns of change

The spatial pattern of the near-surface air temperature change in response to increasing CO_2 is shown in Fig. 21, which shows the annual mean, time-mean differences between the 2X_CO_2 runs and their respective controls for years 91–140 (year 91 is 20 yr after CO_2 has reached twice its initial value). The larger overall warming in CM2.5 (Fig. 21, bottom) is readily apparent, with maximal warming at high latitudes of the Northern Hemisphere.

Several differences are noteworthy. In the North Atlantic there is more warming in CM2.5 than in CM2.1. As will be discussed below, there is a smaller reduction of the AMOC in response to increased CO_2 in CM2.5 than in CM2.1, and hence the poleward oceanic heat transport reduction is smaller in CM2.5. The reduced

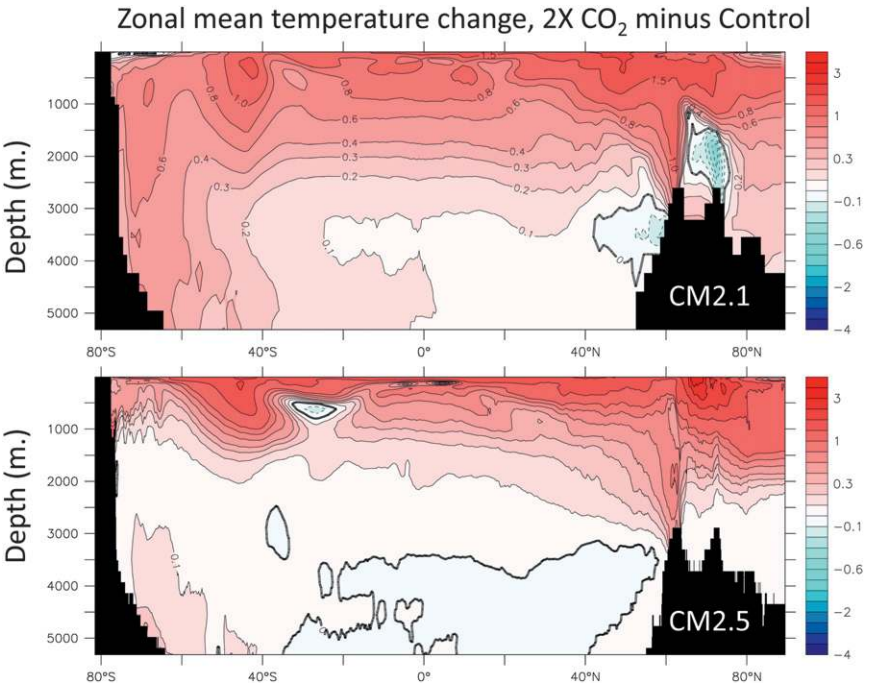

FIG. 22. Zonal mean of temperature change for (a) CM2.1 and (b) CM2.5 between 2X experiment and control run, computed as time mean of temperature in years 91–140 of the 2X experiment minus the corresponding section of the control. Units are K.

poleward oceanic heat transport in CM2.1 offsets a large part of the warming in the subpolar North Atlantic in CM2.1. In contrast, the ocean heat transport reduction in CM2.5 is much smaller, and is thus not able to offset the CO_2-induced warming, resulting in a larger warming in the subpolar North Atlantic in CM2.5.

There is a very notable difference in the high latitudes of the Southern Hemisphere, with much greater near-surface warming south of 45°S in CM2.5 than in CM2.1. The relative minimum in warming in CM2.1 in those latitudes is a common feature of many models, and has been shown to be associated with strong oceanic heat uptake in the Southern Ocean (Meehl et al. 2007, see their Fig. 10.8; Flato and Boer 2001; Manabe et al. 1991). This uptake distributes the warming over a deep vertical section of the Southern Ocean, thereby diminishing the amplitude of surface warming. In contrast, there is strong near-surface warming in the high latitudes of the Southern Hemisphere in CM2.5, along with some warming at depths between 3000 and 5500 m. The subsurface ocean in CM2.5 for this region is not taking up as much heat as in CM2.1. This is shown in Fig. 22, which shows subsurface temperature changes in CM2.5 and CM2.1. The larger penetration of heat in the high latitudes of the Southern Ocean in CM2.1 is readily apparent.

There are at least two possible explanations for this difference. One possibility is that the mean ocean state of CM2.5 in the high latitudes of the Southern Ocean is more stable in the vertical than CM2.1, thereby inhibiting convection and keeping the warming signal near the surface. This stability may arise from processes that have nothing to do with oceanic resolution. Another possibility is that the presence of oceanic eddies significantly modifies the oceanic response to external perturbations. Previous work with an earlier version of a closely related model with similar oceanic resolution (GFDL CM2.4; Farneti et al. 2010; Farneti and Delworth 2010) as well as a high-resolution ocean-only model (Hallberg and Gnanadesikan 2006) shows that the response of the Southern Ocean circulation to enhanced zonal wind stress is sensitive to the treatment of oceanic mesoscale eddies, whether through explicit simulation or a suitable parameterization of their effects (see also Farneti and Gent 2011). Enhanced westerly winds in the Southern Ocean induce a northward Ekman transport of near-surface waters and a steepening of the isopycnals. Farneti et al. (2010) show that in a high-resolution model, the enhanced winds lead to enhanced eddy activity, and that changes in poleward eddy fluxes partially compensate for the enhanced equatorward Ekman transport, leading to weak modifications in local isopycnal slopes. Thus, the response to the enhanced westerly winds is greatly modified and moderated by the presence of oceanic eddies. There exists the possibility that eddies in CM2.5 could modify the

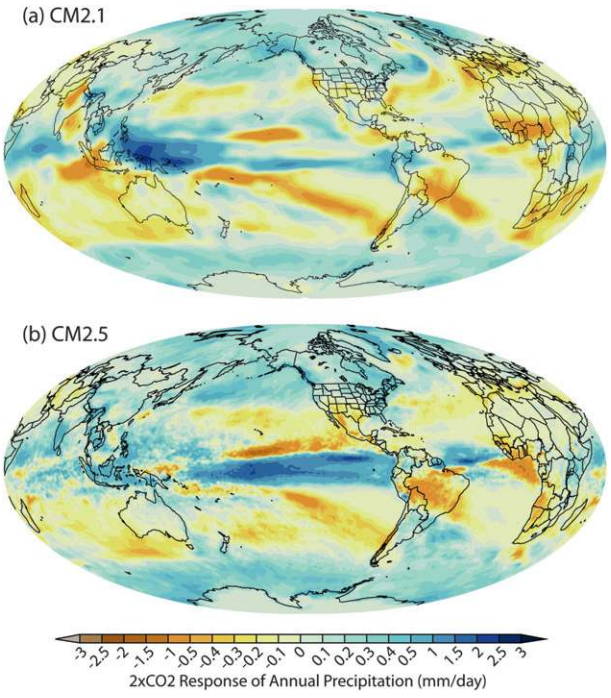

FIG. 23. Map of change in annual mean precipitation (mm day^{-1}) in response to increasing CO_2 for (a) CM2.1 and (b) CM2.5. Maps are computed using data averaged over years 91–140 of the 2X_CO_2 runs minus the corresponding sections of the control runs.

response to CO_2. A complete explanation for the differences in the Southern Ocean warming is beyond the scope of this paper. It is quite possible that the relatively large near-surface warming in the high southern latitudes of CM2.5 is related to the mean state stratification. Future work will examine more carefully the reasons for the large near-surface warming in CM2.5 relative to CM2.1.

The map of annual mean precipitation changes in response to increasing CO_2 is shown in Fig. 23. The broad patterns of enhanced rainfall in parts of the deep tropics, along with high latitudes, and a reduction of precipitation in the subtropics is similar between CM2.1 and CM2.5; this meridional banding of the precipitation response in CM2.5 corresponds to the ''wet get wetter/dry get drier'' pattern that is a robust response across IPCC AR4 climate models (Held and Soden 2006). There are some notable differences, however. For example, while CM2.1 has substantial rainfall reductions over the Sahel (see Held et al. 2005), such reductions are small in CM2.5. There are also larger rainfall reductions over tropical regions of South America in CM2.5 than in CM2.1.

There are substantial differences in projected precipitation changes over southern Europe and the Mediterranean, as shown in Figs. 24b,d. There is a broad area of precipitation reduction over southern Europe and the Mediterranean in CM2.1, consistent with many models used in the IPCC AR4 [see Figs. 10.9 and 10.12 of Meehl et al. (2007)]. In contrast, the reductions in rainfall in CM2.5 are somewhat smaller, are tightly associated with topography, and are largest over mountainous terrain. This represents a different projection of possible rainfall changes over southern Europe and the Mediterranean, and would have a fundamentally different societal impact. Further analysis and experimentation is needed to more thoroughly understand why these precipitation projections differ so substantially between the models, and which is more credible. There are also differences in model projections of precipitation changes over North America (Figs. 24a,c), and their significance and causal factors need to be more carefully examined in future work.

In response to CO_2 doubling, CM2.5 has an enhanced warming of eastern equatorial Pacific surface temperature (Fig. 21), an eastward shift of equatorial Pacific precipitation (Fig. 23), and a weakening of the Pacific Walker circulation (not shown); these precipitation and Walker circulation responses in CM2.5 are also present in most IPCC AR4 models (e.g., Vecchi and Soden 2007; Vecchi and Wittenberg 2010; Collins et al. 2010). There is also enhanced SST warming (Fig. 21) and an associated precipitation increase (Fig. 23) in the western Indian Ocean and equatorial Atlantic; these also resemble the changes seen in the Coupled Model Intercomparison Project 3 (CMIP3) multimodel ensemble (Vecchi and Soden 2007) and may be related to an overall weakening of tropical zonal atmospheric circulation. Though the tropical Pacific response appears ''El Niño–like,'' the western North American precipitation response to CO_2 doubling in CM2.5 deviates substantially from that typically associated with El Niño (Fig. 24c): the drying in southwestern North America and wet conditions in the Pacific Northwest are typical of La Niña conditions (e.g., Larkin and Harrison 2005). In addition, although the tropical Pacific surface temperature and precipitation response of CM2.5 to 2X_CO_2 is more El Niño–like in its structure than that of CM2.1 (Figs. 21, 23), the precipitation response over North America is more La Niña–like in CM2.5 than in CM2.1. These model responses and other recent studies (e.g., Collins 2005; Vecchi and Soden 2007; DiNezio et al. 2010) highlight how El Niño provides an incomplete (possibly misleading) analog for interpreting the character of and mechanisms behind the climatic response to changing radiative forcing.

c. Atlantic meridional overturning circulation

Time series of the AMOC for CM2.1 and CM2.5 are shown in Fig. 25 for both the 1990 control simulations and the 2X_CO_2 simulations. The AMOC in CM2.1 has substantial interdecadal variability with a time scale of

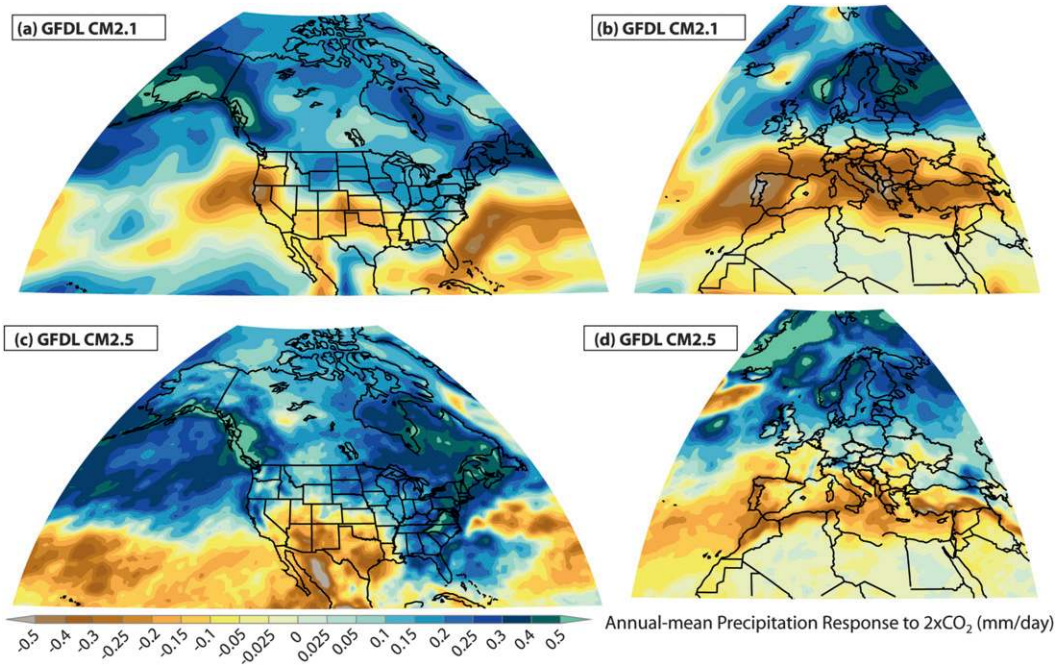

FIG. 24. Map of change in annual mean precipitation (mm day^{-1}) in response to increasing CO_2. Maps are computed using data averaged over years 91–140 of the 2X_CO_2 runs minus the corresponding sections of the control runs. (a) CM2.1 over North America, (b) CM2.1 over Europe and northern Africa, (c) CM2.5 over North America, and (d) CM2.5 over Europe and northern Africa.

approximately 20 yr; in contrast, interdecadal AMOC variability in CM2.5 is rather muted. One hypothesis for this muted interdecadal variability involves a pronounced bias in mixed layer depths in the Labrador Sea where the water is much less stratified than in observations. As a result, convection to depths greater than 3000 m occurs most years in CM2.5, with little interannual variability. This continual deep mixing and lack of interannual variability may serve to mute any AMOC variability and sensitivity to perturbations, since variability and change in Labrador Sea convection are thought to be important factors in AMOC decadal variability and change (see, e.g., Böning et al. 2006). There is substantial multidecadal variability in the Greenland, Iceland, and Norwegian seas in CM2.5, but this signal of variability is not communicated to the North Atlantic.

There are at least two potential reasons for this persistent deep mixing in the Labrador Sea in CM2.5: (i) with no parameterization of the effects of ocean eddies in CM2.5, and with insufficient horizontal resolution to fully resolve eddies in the Labrador Sea, there is relatively weak eddy mixing of the freshwater in the boundary current into the interior of the Labrador Sea. Such transport would help to stratify the Labrador Sea and reduce convection. (ii) As described previously, the resolution of the model is not sufficient to fully represent the flow of dense water over the Denmark and into the deep layers of the Labrador Sea (Winton et al. 1998). This bias leads to warmer and lighter water at depth than observed, also serving to destabilize the water column and enhance wintertime convection. To partially address this bias, a new version of CM2.5 is being developed in which the Denmark Strait and Faroe Bank channel overflows are parameterized using a formulation developed as part of the NOAA–National Science Foundation (NSF)-funded U.S. Climate Process Team (Danabasoglu et al. 2010). Preliminary experiments with this parameterization in both CM2.1 and CM2.5 have shown that it leads to an increase in the amount of cold, dense water in the deeper layers of the Labrador Sea (below 2000 m). There is also a significant reduction in Labrador Sea convection, as measured by mixed layer depth. This parameterization will be employed in a new version of CM2.5 under development.

The reduction of the AMOC in response to increasing CO_2 is somewhat smaller in CM2.5 than in CM2.1, dropping from a mean of around 16 to a little under 14 Sv, for a reduction of approximately 15%. The AMOC in CM2.1 drops from around 20 to about 16 Sv, a reduction of approximately 25%. The smaller AMOC reduction in CM2.5 may be related to the tendency for strong convective mixing each winter in the Labrador Sea. In CM2.1, the upper-ocean warming and freshening in response to increasing CO_2 increase the stratification in the Labrador

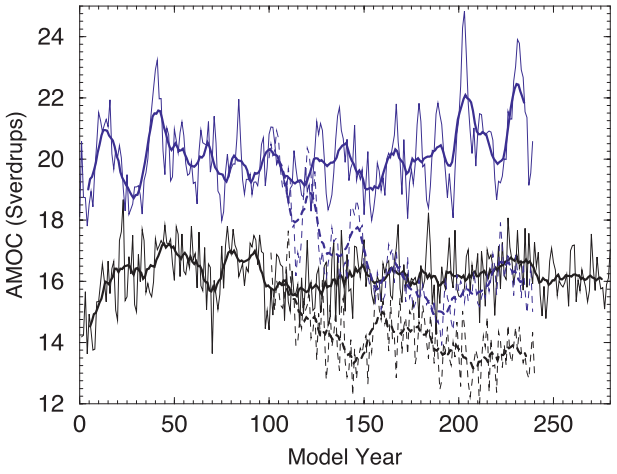

FIG. 25. Time series of the AMOC index for various experiments; the index value is defined as the maximum value in the vertical of the annual mean AMOC field between 20° and 65°N. Thin lines indicate annual mean values, while thick lines are 10-yr running mean time series. Solid black line indicates control simulation from CM2.5, while dashed black line indicates 2X_CO_2 simulation from CM2.5. Solid blue line indicates 1990 control simulation from CM2.1, while dashed blue line indicates 2X_CO_2 simulation from CM2.1.

Sea, thereby reducing convection and weakening the AMOC. The persistent bias in CM2.5 appears to be able to maintain a greater degree of convection, and thus the AMOC reduction is smaller. A more detailed analysis of the differences in the AMOC response to increasing CO_2 is beyond the scope of this paper.

5. Summary and discussion

Improving climate models so that they can provide more robust and credible projections of climate change and variability, particularly on the regional scale, is a critical goal in climate science. Toward this goal, we have presented an overview of the model components and simulation characteristics of GFDL CM2.5. This model is a descendant of the GFDL CM2.1, but uses atmosphere and ocean components with much finer horizontal resolution. The goals are at least twofold: (i) to be able to more faithfully model the effects of smaller-scale processes in the climate system, and (ii) to better simulate climate and its change on regional spatial scales. A specific focus has been the development and incorporation of an ocean component that is far more energetic and realistic than the ocean component of GFDL CM2.1. The strategy to achieve this goal included the use of significantly finer horizontal resolution, a higher-order advection scheme, very low viscosity, and the absence of explicit lateral diffusion.

We present the results from two main simulations with CM2.5, a 280-yr control simulation and a 140-yr idealized climate change simulation. Analysis of the control simulation shows marked improvement in the simulation of many aspects of climate, including on regional scales, relative to the coarser-resolution CM2.1. The simulation of the tropics is notably improved, with substantially reduced biases. Some aspects of ENSO are improved, such as the spatial pattern of variability and associated atmospheric teleconnections, although the time scale is somewhat shorter and more regular than observed. Biases in SST off the west coast of South America and the southwestern coast of North America were virtually eliminated. However, the biases off the west coast of Africa remain, including those in the tropical Atlantic; this occurs despite the improved simulation of South American rainfall. The simulation of the Indian monsoon is substantially improved, as is the precipitation simulation over many continental regions, including South America, North America, and Europe. As measured by the Koppen climate classification system, the relative error in the simulation of continental climate is reduced by 26% in CM2.5 versus CM2.1. The improved representation of orography, both in the atmosphere and ocean, is clearly one important factor in the improved simulation characteristics. Results also point to the importance of explicitly resolving smaller-scale processes, such as oceanic mesoscale eddies, although additional studies are necessary to more thoroughly assess this. One notable deficiency in the current model is a tendency for very deep mixed layers to occur each winter in the Labrador Sea. This is likely related to deficiencies in the representation of overflows of dense water across the sills from the Nordic Seas, as well as weak eddy activity in the Labrador Sea that fails to transport freshwater from the boundary currents into the interior of the Labrador Sea. This is a subject of ongoing work.

Climate change simulations show many similarities with results using the lower-resolution CM2.1, but some intriguing differences emerge. Two of the most significant differences in response to doubled CO_2 are enhanced warming of the near surface in the Southern Ocean in CM2.5 relative to CM2.1, and a change in the precipitation response over the Mediterranean region. In CM2.5, the reduction in precipitation in response to CO_2 is largely associated with topographic features, whereas the precipitation reduction in CM2.1 is more broadscale in character. The CM2.1 results are largely consistent with the ensemble of models assessed in the IPCC AR4.

The primary goals of this paper are to document and describe CM2.5, and to highlight those aspects of the simulations of the control climate and the climate change simulations that are different in CM2.5 versus CM2.1. Detailed analyses of the reasons for these differences will be the subject of future investigations.

Acknowledgments. The authors thank Bruce Wyman, Isaac Held, SJ Lin, and Ming Zhao for assistance with the implementation of their high-resolution atmosphere model within the framework of CM2.5, and Kirsten Findell and Mike Winton for very helpful comments on an earlier version of the manuscript. The authors would also like to thank Amy Langenhorst for help with the FRE software package, and Frank Indiviglio for assistance in facilitating the execution priority of CM2.6. We gratefully acknowledge the very helpful comments of the editor and two anonymous reviewers. The authors wish to acknowledge use of the Ferret program for analysis and graphics in this paper. Ferret is a product of NOAA's Pacific Marine Environmental Laboratory (information available at http://ferret.pmel.noaa.gov/Ferret/).

REFERENCES

Adler, R. F., and Coauthors, 2003: The Version-2 Global Precipitation Climatology Project (GPCP) Monthly Precipitation Analysis (1979–present). *J. Hydrometeor.,* **4,** 1147–1167.

An, S.-I., and B. Wang, 2000: Interdecadal change of the structure of the ENSO mode and its impact on the ENSO frequency. *J. Climate,* **13,** 2044–2055.

Annamalai, H., K. Hamilton, and K. R. Sperber, 2007: South Asian summer monsoon and its relationship with ENSO in the IPCC AR4 simulations. *J. Climate,* **20,** 1071–1092.

Antonov, J. I., S. Levitus, T. P. Boyer, M. E. Conkright, T. D. O'Brien, and C. Stephens, 1998: *Temperature of the Atlantic Ocean*. Vol. 1, *World Ocean Atlas 1998,* NOAA Atlas NESDIS 27, 166 pp.

Böning, C. W., M. Scheinert, J. Dengg, A. Biastoch, and A. Funk, 2006: Decadal variability of subpolar gyre transport and its reverberation in the North Atlantic overturning. *Geophys. Res. Lett.,* **33,** L21S01, doi:10.1029/2006GL026906.

Boyer, T. P., S. Levitus, J. I. Antonov, M. E. Conkright, T. D. O'Brien, and C. Stephens, 1998: *Salinity of the Atlantic Ocean*. Vol. 4, *World Ocean Atlas 1998,* NOAA Atlas NESDIS 30, 166 pp.

Bryan, F. O., R. Tomas, J. M. Dennis, D. B. Chelton, N. G. Loeb, and J. L. McClean, 2010: Frontal-scale air–sea interaction in high-resolution coupled climate models. *J. Climate,* **23,** 6277–6291.

Capotondi, A., A. Wittenberg, and S. Masina, 2006: Spatial and temporal structure of tropical Pacific interannual variability in 20th century coupled simulations. *Ocean Modell.,* **15,** 274–298.

Colella, P., and P. R. Woodward, 1984: The Piecewise Parabolic Method (PPM) for gas-dynamical simulations. *J. Comput. Phys.,* **54,** 174–201.

Collins, M., 2005: El Niño- or La Niña-like climate change? *Climate Dyn.,* **24,** 89–104.

——, and Coauthors, 2010: The impact of global warming on the tropical Pacific and El Niño. *Nat. Geosci.,* **3,** 391–397, doi:10.1038/ngeo868.

Cunningham, S. A., S. G. Alderson, B. A. King, and M. A. Brandon, 2003: Transport and variability of the Antarctic Circumpolar Current in Drake Passage. *J. Geophys. Res.,* **108,** 8084, doi:10.1029/2001JC001147.

Danabasoglu, G., W. G. Large, and B. P. Briegleb, 2010: Climate impacts of parameterized Nordic Sea overflows. *J. Geophys. Res.,* **115,** C11005, doi:10.1029/2010JC006243.

Delworth, T. L., and Coauthors, 2006: GFDL's CM2 global coupled climate models. Part I: Formulation and simulation characteristics. *J. Climate,* **19,** 643–674.

DiNezio, P., A. Clement, and G. A. Vecchi, 2010: Reconciling differing views of tropical Pacific climate change. *Eos, Trans. Amer. Geophys. Union,* **91,** doi:10.1029/2010EO160001.

Farneti, R., and T. L. Delworth, 2010: The role of mesoscale eddies in the remote oceanic response to altered Southern Hemisphere winds. *J. Phys. Oceanogr.,* **40,** 2348–2354.

——, ——, A. J. Rosati, S. M. Griffies, and F. Zeng, 2010: The role of mesoscale eddies in the rectification of the Southern Ocean response to climate change. *J. Phys. Oceanogr.,* **40,** 1539–1557.

——, and P. R. Gent, 2011: The effects of the eddy-induced advection coefficient in a coarse-resolution coupled climate model. *Ocean Modell.,* **39,** 135–145, doi:10.1016/j.ocemod.2011.02.005.

Flato, G. M., and G. J. Boer, 2001: Warming asymmetry in climate change simulations. *Geophys. Res. Lett.,* **28,** 195–198.

Fox-Kemper, B., and Coauthors, 2011: Parameterization of mixed layer eddies. III: Implementation and impact in global ocean climate simulations. *Ocean Modell.,* **39,** 61–78, doi:10.1016/j.ocemod.2010.09.002.

Gent, P. R., S. G. Yeager, R. B. Neale, S. Levis, and D. A. Bailey, 2010: Improvements in a half degree atmosphere/land version of the CCSM. *Climate Dyn.,* **34,** 819–833.

GFDL Global Atmospheric Model Development Team, 2004: The new GFDL global atmosphere and land model AM2–LM2: Evaluation with prescribed SST simulations. *J. Climate,* **17,** 4641–4673.

Gnanadesikan, A., and R. J. Stouffer, 2006: Diagnosing atmosphere-ocean general circulation model errors relevant to the terrestrial biosphere using the Köppen climate classification. *Geophys. Res. Lett.,* **33,** L22701, doi:10.1029/2006GL028098.

——, and Coauthors, 2006: GFDL's CM2 Global Coupled Climate Models. Part II: The baseline ocean simulation. *J. Climate,* **19,** 675–697.

Griffies, S. M., 2010: Elements of MOM4P1. GFDL Ocean Group Tech. Rep. 6, NOAA/Geophysical Fluid Dynamics Laboratory, 444 pp. [Available online at http://www.gfdl.noaa.gov/fms.]

——, and R. W. Hallberg, 2000: Biharmonic friction with a Smagorinsky-like viscosity for use in large-scale eddy-permitting ocean models. *Mon. Wea. Rev.,* **128,** 2935–2946.

——, and Coauthors, 2005: Formulation of an ocean model for global climate simulations. *Ocean Sci.,* **1,** 45–79.

——, and Coauthors, 2009: Coordinated Ocean-ice Reference Experiments (COREs). *Ocean Modell.,* **26,** 1–46, doi:10.1016/j.ocemod.2008.08.007.

——, and Coauthors, 2011: GFDL's CM3 coupled climate model: Characteristics of the ocean and sea ice simulations. *J. Climate,* **24,** 3520–3544.

Guilyardi, E., A. Wittenberg, A. Fedorov, M. Collins, C. Wang, A. Capotondi, G. J. van Oldenborgh, and T. Stockdale, 2009: Understanding El Niño in ocean–atmosphere general circulation models: Progress and challenges. *Bull. Amer. Meteor. Soc.,* **90,** 325–340.

Hallberg, R., and A. Gnanadesikan, 2006: The role of eddies in determining the structure and response of the wind-driven Southern Hemisphere overturning: Results from the Modeling Eddies in the Southern Ocean (MESO) project. *J. Phys. Oceanogr.,* **36,** 2232–2252.

Held, I. M., and B. J. Soden, 2006: Robust responses of the hydrological cycle to global warming. *J. Climate,* **19,** 5686–5699.

——, T. L. Delworth, J. Lu, K. Findell, and T. R. Knutson, 2005: Simulation of Sahel drought in the 20th and 21st centuries. *Proc. Natl. Acad. Sci. USA,* **102,** 17 891–17 896, doi:10.1073/pnas.0509057102.

Hunke, E. C., and J. K. Dukowicz, 1997: An elastic-viscous-plastic model for sea ice dynamics. *J. Phys. Oceanogr.,* **27,** 1849–1867.

Huynh, H. T., 1996: Schemes and constraints for advection. *Fifteenth International Conference on Numerical Methods in Fluid Dynamics,* P. Kutler, J. Flores, and J.-J. Chattot, Eds., Lecture Notes in Physics, Vol. 490, Springer, 498–503.

Johns, W. E., and Coauthors, 2011: Continuous, array-based estimates of Atlantic Ocean heat transport at 26.5°N. *J. Climate,* **24,** 2429–2449.

Kalnay, E., and Coauthors, 1996: The NCEP/NCAR 40-Year Reanalysis Project. *Bull. Amer. Meteor. Soc.,* **77,** 437–471.

Kanzow, T., and Coauthors, 2010: Seasonal variability of the Atlantic meridional overturning circulation at 26.5°N. *J. Climate,* **23,** 5678–5698.

Kim, D., J.-S. Kug, I.-S. Kang, F.-F. Jin, and A. T. Wittenberg, 2008: Tropical Pacific impacts of convective momentum transport in the SNU coupled GCM. *Climate Dyn.,* **31,** 213–226.

Kirtman, B. P., 1997: Oceanic Rossby wave dynamics and the ENSO period in a coupled model. *J. Climate,* **10,** 1690–1704.

Kistler, R., and Coauthors, 2001: The NCEP–NCAR 50-Year Reanalysis: Monthly means CD-ROM and documentation. *Bull. Amer. Meteor. Soc.,* **82,** 247–267.

Kottek, M., J. Grieser, C. Beck, B. Rudolf, and F. Rubel, 2006: World map of the Koppen climate classification updated. *Meteor. Z.,* **15,** 259–263.

Kug, J.-S., J. Choi, S.-I. An, F.-F. Jin, and A. T. Wittenberg, 2010: Warm pool and cold tongue El Niño events as simulated by the GFDL CM2.1 coupled GCM. *J. Climate,* **23,** 1226–1239.

Large, W. G., J. C. McWilliams, and S. C. Doney, 1994: Oceanic vertical mixing: A review and a model with a nonlocal boundary layer parameterization. *Rev. Geophys.,* **32,** 363–403.

Larkin, N. K., and D. E. Harrison, 2005: On the definition of El Niño and associated seasonal average U.S. weather anomalies. *Geophys. Res. Lett.,* **32,** L13705, doi:10.1029/2005GL022738.

Lee, H.-C., A. Rosati, and M. J. Spelman, 2006: Barotropic tidal mixing effects in a coupled climate model: Oceanic conditions in the North Atlantic. *Ocean Modell.,* **11,** 467–477.

Legates, D. R., and C. J. Willmott, 1990: Mean seasonal and spatial variability in gauge-corrected, global precipitation. *Int. J. Climatol.,* **10,** 111–127.

Le Traon, P.-Y., F. Nadal, and N. Ducet, 1998: An improved mapping method of multisatellite altimeter data. *J. Atmos. Oceanic Technol.,* **15,** 522–534.

Lin, S.-J., 2004: A ''vertically Lagrangian'' finite-volume dynamical core for global models. *Mon. Wea. Rev.,* **132,** 2293–2307.

Manabe, S., R. J. Stouffer, M. J. Spelman, and K. Bruan, 1991: Transient responses of a coupled ocean-atmosphere model to gradual changes of atmospheric CO_2. Part I: Annual mean response. *J. Climate,* **4,** 785–818.

Martin, T, and A. Adcroft, 2010: Parameterizing the fresh-water flux from land ice to ocean with interactive icebergs in a coupled climate model. *Ocean Modell.,* **34,** 111–124, doi:10.1016/j.ocemod.2010.05.001.

McClean, J. L., and Coauthors, 2011: A prototype two-decade fully-coupled fine-resolution CCSM simulation. *Ocean Modell.,* **39,** 10–30, doi:10.1016/j.ocemod.2011.02.011.

Meehl, G. A., and Coauthors, 2007: Global climate projections. *Climate Change 2007: The Physical Science Basis,* S. Solomon et al., Eds., Cambridge University Press, 747–846.

Milly, P. C. D., and A. B. Shmakin, 2002: Global modeling of land water and energy balances. Part I: The Land Dynamics (LaD) model. *J. Hydrometeor.,* **3,** 283–299.

Minobe, S., A. Kuwano-Yoshida, N. Komori, S.-P. Xie, and R. J. Small, 2008: Influence of the Gulf Stream on the troposphere. *Science,* **452,** 206–209, doi:10.1038/Nature06690.

Murray, R. J., 1996: Explicit generation of orthogonal grids for ocean models. *J. Comput. Phys.,* **126,** 251–273.

Pacanowski, R. C., 1987: Effect of equatorial currents on surface stress. *J. Phys. Oceanogr.,* **17,** 833–838.

Perovich, D., T. C. Grenfell, B. Light, and P. V. Hobbs, 2002: Seasonal evolution of the albedo of multiyear Arctic sea ice. *J. Geophys. Res.,* **107,** 8044, doi:10.1029/2000JC000438.

Putman, W. M., and S.-J. Lin, 2007: Finite-volume transport on various cubed-sphere grids. *J. Comput. Phys.,* **227,** 55–78.

Rajeevan, M., and R. S. Nanjundiah, 2009: Coupled model simulations of twentieth century climate of the Indian summer monsoon. *Current Trends in Science: Platinum Jubilee Special,* N. Mukunda, Ed., Indian Academy of Sciences, 537–568.

Shaffrey, L. C., and Coauthors, 2009: U.K. HiGEM: The new U.K. High-Resolution Global Environment Model—Model description and basic evaluation. *J. Climate,* **22,** 1861–1896.

Simmons, H. L., S. R. Jayne, L. C. St. Laurent, and A. J. Weaver, 2004: Tidally driven mixing in a numerical model of the ocean general circulation. *Ocean Modell.,* **6,** 245–263.

Smith, T. M., R. W. Reynolds, T. C. Peterson, and J. Lawrimore, 2008: Improvements to NOAA's historical merged land–ocean surface temperature analysis (1880–2006). *J. Climate,* **21,** 2283–2296.

Steele, M., R. Morfley, and W. Ermold, 2001: PHC: A global ocean hydrography with a high-quality Arctic Ocean. *J. Climate,* **14,** 2079–2087.

Vecchi, G. A., and B. J. Soden, 2007: Global warming and the weakening of the tropical circulation. *J. Climate,* **20,** 4316–4340.

——, and A. T. Wittenberg, 2010: El Niño and our future climate: Where do we stand? *Wiley Interdiscip. Rev.: Climate Change,* **1,** 260–270, doi:10.1002/wcc.33.

Winton, M., 2000: A reformulated three-layer sea ice model. *J. Atmos. Oceanic Technol.,* **17,** 525–531.

——, R. W. Hallberg, and A. Gnanadesikan, 1998: Simulation of density-driven frictional downslope flow in z-coordinate ocean models. *J. Phys. Oceanogr.,* **28,** 2163–2174.

Wittenberg, A. T., 2002: ENSO response to altered climates. Ph.D. thesis, Princeton University, 475 pp.

——, 2009: Are historical records sufficient to constrain ENSO simulations? *Geophys. Res. Lett.,* **36,** L12702, doi:10.1029/2009GL038710.

——, A. Rosati, N.-C. Lau, and J. J. Ploshay, 2006: GFDL's CM2 global coupled climate models. Part III: Tropical Pacific climate and ENSO. *J. Climate,* **19,** 698–722.

Xie, P., and P. A. Arkin, 1997: Global precipitation: A 17-year monthly analysis based on gauge observations, satellite estimates, and numerical model outputs. *Bull. Amer. Meteor. Soc.,* **78,** 2539–2558.

Zhang, R., T. L. Delworth, A. Rosati, W. G. Anderson, K. W. Dixon, H.-C. Lee, and F. Zeng, 2011: Sensitivity of the North Atlantic Ocean circulation to an abrupt change in the Nordic Sea overflow in a high resolution global coupled climate model. *J. Geophys. Res.,* **116,** C12024, doi:10.1029/2011JC007240.